Emerging Techniques in Breast MRI

Anum S. Kazerouni[1], Adrienne N. Dula[2], Angela M. Jarrett[3,4], Guillermo Lorenzo[3,5], Jared A. Weis[6], James A. Bankson[7], Eduard Y. Chekmenev[8], Federico Pineda[9], Gregory S. Karczmar[9], Thomas E. Yankeelov[3,4,7,10]

[1]Department of Radiology
University of Washington
Seattle, Washington 98195

[2]Department of Neurology
The University of Texas at Austin
Austin, Texas 78712

[3]Oden Institute for Computational Engineering and Sciences,
The University of Texas at Austin
Austin, Texas 78712

[4]Livestrong Cancer Institutes
The University of Texas at Austin
Austin, Texas 78712

[5]Department of Civil Engineering and Architecture
University of Pavia
27100 Pavia, Italy

[6]Department of Biomedical Engineering
Wake Forest School of Medicine
Winston-Salem, North Carolina 27101

[7]Department of Imaging Physics
The University of Texas MD Anderson Cancer Center
Houston, Texas 77030

[8]Department of Chemistry,
Karmanos Cancer Institute
Integrative Biosciences
Wayne State University
Detroit, Michigan 48202
Russian Academy of Sciences, Leninskiy Prospekt 14
Moscow, 119991, Russia

[9]Department of Radiology
The University of Chicago
Chicago, Illinois 60637

[10]Departments of Biomedical Engineering, Diagnostic Medicine, and Oncology
The University of Texas at Austin
Austin, Texas 78712

Abstract.

As indicated throughout this text, there is a constant effort to move to more sensitive, specific, and quantitative methods for characterizing breast tissue *via* magnetic resonance imaging (MRI). In the present chapter, we focus on six emerging techniques that seek to quantitatively interrogate the physiological and biochemical properties of the breast. At the physiological scale, we present an overview of ultra-fast dynamic contrast enhanced MRI and magnetic resonance elastography which provide remarkable insights into the vascular and mechanical properties of tissue, respectively. Moving to the biochemical scale, magnetization transfer, chemical exchange saturation transfer, and spectroscopy (both "conventional" and hyperpolarized) methods all provide unique, non-invasive, insights into tumor metabolism. Given the breadth and depth of information that can be obtained in a single MRI session, methods of data synthesis and interpretation must also be developed. Thus, we conclude the chapter with an introduction to two very different, though complementary, methods of data analysis: 1) radiomics and habitat imaging, and 2) mechanism-based mathematical modeling.

Key words. Quantitative MRI, ultra-fast MRI, magnetic resonance spectroscopy, magnetization transfer, chemical exchange saturation transfer, hyperpolarized MRI, mathematical modeling

1. Introduction.

Magnetic resonance imaging (MRI) is clinically utilized to evaluate patient prognosis, extent of disease, and therapeutic response for patients with breast cancer. All three of these applications of breast MRI, within the standard-of-care setting, are dominated by anatomical and morphological based imaging. However, as anatomical and morphological assessments are fundamentally limited in their ability to characterize the underlying physiological, cellular, and molecular changes within tissue, they can be inadequate in many contexts of patient care. Thus, there has been great effort (over many years) to develop MRI-based measures that can accurately and precisely characterize the relevant tumor biology of breast lesions. The subject of this chapter is to provide an introduction, and illustrative examples, of a range of emerging MRI-based techniques that are designed to quantitatively report on breast tissue at the physiological, cellular, and molecular levels. At the physiological scale, topics discussed include hemodynamics (ultra-fast contrast enhanced MRI), architecture (MR elastography), and macromolecular content (magnetization transfer and chemical exchange saturation transfer MRI). At the cellular and molecular levels, we present insights from metabolites known to be present at higher concentrations in malignant cells (MR spectroscopy) as well as methods to characterize metabolism (hyperpolarized MRI). The chapter is concluded with a description of two techniques for analyzing and summarizing the enormous amount of multi-parametric data that emerges from modern MRI studies, one based on a data-driven approach (radiomics), and another that attempts to explicitly model the underlying biology (mechanism-based, mathematical modeling).

2. Ultra-fast dynamic contrast enhanced imaging

Standard-of-care MR images are acquired at very high spatial resolution to characterize patient anatomy and tumor morphology. This requires scan times of 60-90 seconds which is far too low to accurately measure kinetic parameters, especially in early uptake phase when signal changes rapidly, particularly in cancers. This means that important diagnostic and prognostic information is lost. Lesion conspicuity is highest immediately after contrast injection[1,2], so it is especially important to faithfully capture early-uptake kinetics. Other modes of analysis, including

analysis of morphology, also benefit from increased temporal resolution. Texture features have typically been viewed as static, but recent work[3,4] has shown improvement in diagnostic efficacy when the evolution of texture over time is analyzed[5,6].

Pharmacokinetic analysis requires quantitative measurement of the arterial input function (AIF) with high temporal resolution. In a seminal study, Henderson *et al*.[7] recommended that the AIF should be measured with temporal resolution of 1 s/image; a challenging task, indeed. Parker *et al*.[8] defined a population-average AIF with resolution of 5s/image. In small animals, researchers have characterized AIFs with significantly higher sampling frequency: Yankeelov *et al*.[9] measured an AIF at 0.9s/image in mice, while Kershaw *et al*. measured an AIF at 0.44s/image in rabbits[10]. This previous work demonstrates that temporal resolution much higher than that employed in the routine, clinical DCE-MRI study is required to maximize diagnostic accuracy.

There are a number of approaches currently under investigation to accelerate the acquisition of DCE-MRI. Ultrafast methods using conventional partial Fourier sampling, and high parallel imaging acceleration can be used to image the early phase of contrast media uptake in the breast at high temporal resolution[11-13]. View-sharing methods[14-19] accelerate acquisitions by sampling *k*-space with non-uniform densities, sampling low frequencies much more often than high spatial frequencies. While these methods accurately represent large-scale enhancement patterns (e.g., average enhancement within a lesion), they sample different spatial frequencies at different temporal resolutions which can lead to errors in any subsequent analysis. Compressed sensing[15,20-24] leverages sparse enhancement during the early phase of contrast media uptake to create L_1-constrained image reconstructions from very highly under-sampled data. This provides high spatial and temporal resolution. However, the incoherent *k*-space sampling can cause ghosting and signal blurring artifacts. Learning-based methods[25,26] produce image reconstructions based on repeated training with large numbers of datasets. These methods have potential for high acceleration combined with good spatial resolution. However, the reconstruction process is a "black box", and it is difficult characterize the artifacts it produces. Furthermore, features not found in the training set are difficult to identify in individual patients found in the "validation" or test case(s). Finally, the unfolding method[27] accelerates bilateral breast DCE-MRI by reducing the field-of-view, allowing aliasing, and unfolding the resulting images. Since less than 5% of voxels enhance significantly during the first 30 - 45 seconds after injection, enhancing voxels rarely overlap in aliased images.

Ultrafast DCE-MRI is commonly based on a spoiled gradient echo pulse sequence with minimized *TR* and *TE*, often with fat suppression. Ultrafast sampling can be incorporated into a standard clinical protocol, as shown in **Figure 1**. The top line in blue shows a conventional clinical DCE-MRI protocol with 60 second acquisitions before and after contrast injection. In the bottom scheme, ultrafast acquisitions are inserted for 30 seconds before and 45 seconds after contrast injection. This is followed by 60-second high spatial resolution acquisitions to follow contrast media washout. Ultrafast sampling allows accurate sampling of a number of important parameters:

a. Arterial input function. With high temporal resolution, the initial portion of the AIF can be calculated directly from the internal mammary artery using only the early portion of the contrast bolus, when the contrast media concentrations in the blood are relatively low and can be accurately measured by MRI. Alternatively, with a low dose of contrast media, the entire AIF can be measured directly from an artery[2,28].

b. Bolus tracking. The peak of the contrast media bolus can be tracked through the arteries to trace blood vessels and measure arterial and venous blood flow[2,29]. Preferably, these measurements would be performed with sampling at 2 sec^{-1} or higher, but even resolutions of 0.3 sec^{-1} provides useful information.

c. Unidirectional K^{trans} measurement. Ultrafast sampling allows accurate measurement of the early phase of contrast media uptake. In this case a unidirectional model can be used for pharmacokinetic analysis. This approximates that flow occurs only from plasma to the extravascular space, and there is no backflow. This avoids errors due to the use of compartmental models that may not be applicable to breast tissue[30,31].

d. The bolus arrival time (BAT) or time-of-initial enhancement (TIE). The BAT in arteries and TIE in tissue are important markers for cancer[14,28] that can be accurately measured from ultrafast data. Values for BAT and TIE should be expressed relative to the time of initial enhancement in the aorta to remove the influence of global variables such as cardiac output.

e. Lesion transit time (LTT). High temporal resolution data makes it possible to identify arteries feeding suspicious lesions and veins draining the lesions, based on differences in BAT. This allows calculation of the LTT (see **Figure 2**).

The introduction of ultrafast imaging allows precise measurement of the initial enhancement in arteries, veins, normal breast tissue, and cancers. These new kinetic parameters (i.e., TIE and BAT) show great promise for increasing diagnostic accuracy[2,14]. Mann *et al*. showed

that the 'TIE' measured using a view sharing method (TWIST) was more effective than the conventional BIRADS 'curve type' analysis[14,15] in distinguishing benign from enhancing abnormalities. Pineda *et al*. developed a 'low-dose imaging technique' (LITE) that uses 15% of the standard dose, combined with ultrafast sampling. They showed that ultrafast DCE-MRI could detect lesions reliably at the low dose, and in fact conspicuity and enhancement rate were both higher in the low-dose images, with low-to-standard-dose ratios of 1.5 ± 0.1 and 1.2 ± 0.4, respectively. This suggests that ultrafast LITE DCE-MRI measures contrast agent dynamics accurately and with high dynamic range[28,32]. The LITE ultrafast approach has potential to reduce adverse effects of contrast agents, increase screening compliance, and improve quantitative analysis.

While development and clinical implementation of ultrafast methods for breast DCE-MRI are at an early stage, it is reasonable to expect significant advances in sampling rate and spatial resolution. This new approach to DCE-MRI is leading to new methods for quantitative analysis as well as new diagnostic and prognostic parameters (see, e.g., ref. 33) that will facilitate more widespread and effective clinical use of MRI for breast cancer screening.

3. Magnetic Resonance Elastography

Magnetic resonance elastography (MRE) quantitatively interrogates the mechanical integrity of tissue, with image contrast derived from mechanical properties of tissue. MRE can characterize fundamental functional mechanical properties of tissues, thereby providing important insights into tissue disease status, as changes in the composition and cytoarchitecture of tissue often accompany disease progression. Specifically, distinct changes in the tissue mechanical microenvironment are associated with breast cancer progression. Alterations of the breast tumor stroma to increase the deposition, structural remodeling, and organization of extracellular matrix (ECM) proteins are observed as a part of a desmoplastic transition that has been shown to have roles as both a host reaction to tumor invasion as well as facilitating further tumor aggressiveness[34-38]. This transition to an aberrant ECM state is associated with dramatic increases in tissue mechanical stiffness properties[39]. Clinical examination of breast disease commonly exploits this physical phenomenon, relying on detection of aberrant mechanical stiffness of breast tissue through manual palpation. MRE, as a direct and functional non-invasive measure of mechanical stiffness, seeks to quantitatively characterize changes in breast tissue mechanical properties as an

indicator of tissue abnormalities. Indeed, recent preclinical studies comparing MRE with computational histology have shown that MRE provides an accurate measure of tumor collagen status that is sensitive to therapeutic ECM modulation[40].

MRE characterizes tissue mechanical properties through the analysis of image acquisitions that are synchronized with externally applied or intrinsically activated mechanical loading. Following induction of deformation, acquired images record the tissue mechanical displacement response to the deformation loading. The displacement images can then be post-processed to yield spatial maps of mechanical elasticity based on assumed relationships between the physical constitutive mechanical material properties. While MRE initially emerged as an imaging method to non-invasively measure mechanical elasticity, MRE techniques have been extended beyond the elasticity namesake to examine various additional mechanical phenotypic properties to characterize other tissue mechanical properties, such as anisotropy, viscoelasticity, hyperelasticity, and poroelasticity[41-44].

There are a number of MRI-based measurement of breast tissue mechanical properties that differ based on the selected mechanical deformation source, displacement image acquisition, and mechanical property inversion method. In dynamic MRE, vibrational piezoelectric or acoustic drivers are placed in direct contact with either the breast or sternum and used to induce mechanical shear waves within breast tissue. Phase-contrast MRI techniques are sensitive to induced displacement using oscillating motion encoding gradient sequences that are synchronized to the frequency of vibrational mechanical loading and used to record displacement wave propagation. Based on an assumption of constitutive property relationship between displacement and mechanical properties, elastic and/or viscoelastic mechanical properties are estimated by processing of the wave displacement image using computational models or analytical direct inversion methods. In quasi-static MRE, MR images are acquired in differing states of tissue deformation, either externally induced or intrinsically activated. Tissue mechanical elasticity properties are then estimated by computational model processing of either MR spin-tagging/strain-encoding images[45], or non-rigid image registration techniques applied to conventional anatomical images[46]. An example of quasi-static MRE in breast cancer with model-based estimation of tissue mechanical elasticity properties is shown in **Figure 3**.

MRE is an emerging technique in breast imaging and as such there are a limited number of studies applying MRE in the breast. In these preliminary studies, MRE has shown promise for

use in multi-parametric imaging assessment of breast disease. In a study by Balleyguier *et al*., MRE was used to assess the viscoelasticity of suspicious breast lesions in 43 patients with the goal of predicting malignancy status[47]. Viscoelasticity mechanical properties determined by MRE were found to correlate with MRI BI-RADS score and subsequent histological assessment. Prediction of lesion malignancy status by combining MRE viscoelasticity phase angle with the MRI BI-RADS score was found to improve the diagnostic accuracy over BI-RADS scoring alone, increasing the area under the receiver operating characteristic curve from 0.84 to 0.92[47]. In another study by Hawley *et al*., breast MRE assessed stiffness was found to scale with the amount of fibroglandular tissue, with dense breasts associated with significantly increased stiffness as compared to nondense breasts. Additionally, Hawley *et al*. performed reproducibility studies for breast MRE in 22 healthy volunteers. Breast MRE mechanical properties were found to be significantly reproducible with concordance correlation coefficient of 0.87 and 95% limits of agreement of -0.11 to 0.12 kPa over a range of mean stiffness from 0.6 to 1.2 kPa for central slice analysis of breast stiffness[48]. Whole breast analysis of stiffness showed reproducibility with concordance correlation coefficient of 0.91 and 95% limits of agreement of -0.07 to 0.09 kPa over a range of mean stiffness from 0.6 to 1.1 kPa[48]. For a thorough review of dynamic MRE applied to the breast, the interested reader is referred to published reviews[49, 50].

4. Magnetization Transfer and Chemical Exchange Saturation Transfer

Biological tissue includes freely moving water molecules, which can be examined by standard MRI techniques, as well as a *milieu* of other molecules within the extracellular matrix such as proteins, peptides, glycoproteins, including collagen, laminin, proteoglycans, and fibronectin. Indirect detection of the energy transfer between these macromolecules and the free water allows characterization of this complex molecular environment using magnetization transfer (MT) and chemical exchange saturation transfer (CEST) MRI. MT-MRI reports on the macromolecular content of tissue in a semi-solid or bound state[51], while CEST-MRI reflects more mobile macromolecules[52, 53] (potential indicators of pH[54] and cellular levels of mobile proteins and peptides). These saturation-based imaging methods have both demonstrated the potential for tumor detection, characterization, and treatment assessment[55-62]. By measuring the biochemical composition of tissues, MT- and CEST-MRI are able to probe the complex molecular environment and provide complementary information to standard, anatomical MRI.

Magnetization transfer exploits the interactions between water protons within two distinct environments. This "two-pool" model is based on the "free" water proton pool, which produces the conventionally-visible MRI signal, and a "bound" proton pool in which the protons are bound to macromolecules (**Figure 4**) [63]. Exchange and cross-relaxation of magnetization between these two pools give rise to the MT effect[51], resulting in attenuated signal intensity when the bound protons are saturated well off-resonance[63, 64]. The protons of the semi-solid tissue components (e.g., membranes and collagen) have very short T_2 and high degree of coupling and can therefore transfer saturation rapidly, resulting in a reduced MR signal.

Chemical exchange is a type of MT in which protons of mobile macromolecules, such as proteins and peptides, directly exchange with the free water. These exchangeable protons, resonating at discrete frequencies relatively close to water, can be quantified through selective saturation and delayed detection of the water signal, which is affected by the transfer of this saturation.

MT-MRI is based on observing the effects of far off-resonance radio-frequency (RF) pulses on the measured the signal intensity. This off-resonance irradiation can be applied in a continuous wave or pulsed mode[65] prior to spoiled gradient echo acquisition (**Figure 5**). Importantly, MT measurements do not report directly on tissue properties, but rather reflect the experimental settings related to saturation (power, offset frequency, and duty cycle) and the image acquisition (repetition time [TR], echo time [TE], and flip angle). This semi-quantitative imaging technique is typically accomplished using a 2D or 3D spoiled gradient-echo sequence with excitation, preceded by saturation preparation with a bandwidth of a few 100 Hz, at a single frequency offset ($\Delta\omega$) between 50 Hz-50 kHz from the free proton resonance (Figure 5). The pulse amplitude and duration are typically governed by specific absorption rate (SAR) limitations.

While conventional MT-MRI includes a minimum of two images acquired, with- and without saturation, CEST-MRI extends the idea of MTR to implement selective RF irradiation through a range of frequencies proximal to water ($\Delta\omega$ = 1.5 ppm for hydroxyls and 3.5 ppm for amides) [52, 53, 66]. The CEST effect depends on many factors such as field strength ($\boldsymbol{B}_0$), concentration of exchanging protons, exchange rate (k_{bf}), field homogeneities (both $\boldsymbol{B}_0$ *and* $\boldsymbol{B}_1$), T_1 of water protons, and RF saturation pulse duration (τ_d), duty cycle, and amplitude, which may be optimized for a given metabolite. Saturation in CEST-MRI of the breast is typically achieved *via* a series of RF pulses followed by a fast-imaging technique (**Figure 6**) to accommodate image

acquisitions needed to sample the spectral offsets (n > 30) and the long saturation time needed (order of seconds).

Initial applications of MT-MRI in the breast demonstrated its feasibility, reproducibility, and repeatability in the clinical setting[67, 68]. Application in patient populations have revealed significant reductions in the MTR in malignant lesions compared to benign[55, 56], potentially reflecting differences in structure of the collagenous component of the extra-cellular matrix. This is corroborated by the work of Virostko *et al*.[68] in which longitudinal evaluation of patients during neoadjuvant chemotherapy (NAT) suggested that a decline in the average MTR of the lesion correspond to therapeutic response (Figure 5A). Further evaluation of the distribution of MTR values within breast lesions indicated a wider distribution of tumor MTR values in patients who achieved a pathological complete response after 2–4 cycles of NAT compared to non-responders[68]. Together these studies support prognostic potential for MTR in the NAT setting.

CEST MRI of the amide proton transfer (APT), as well as glycosaminoglycans (gagCEST), have been shown to be feasible and reproducible at both 7T[59] and 3T[61]. CEST-MRI measurements of APT have been performed in patients before and after one cycle of chemotherapy (**Figure 7**). Following therapy, APT increased in the one patient with progressive disease and decreased in the two patients with a partial or complete response suggesting that CEST-MRI may report on treatment response in these patients[61].

5. Magnetic Resonance Spectroscopy

Conventional proton magnetic resonance spectroscopy (MRS) is a noninvasive approach to detect and quantify metabolites *in vivo*. The spectrum is collected from a voxel, which can be localized in various homogeneous parts of the human body including breast. Most clinically useful metabolites resonate at proton chemical shifts ranging from 1 to 5 ppm including water. As the metabolites' concentration is typically in the range of 1-20 mM, MRS faces two fundamental challenges. The first one is the size of the voxel that is required to obtain spectra with sufficient signal-to-noise ratio—the voxel size is large: ~2-3 orders of magnitude greater than the voxel size in conventional standard-of-care MRI scan. Second, a water suppression is required to minimize the background signal of water in MRS. Despite these challenges many metabolites can be detected *in vivo*[69]. Lactate and choline proton resonances have been employed as diagnostic markers for a

wide range of diseases for the purpose of initial diagnosis and monitoring response to treatment[70, 71].

The additional MRS challenges in breast are tissue heterogeneity and the substantial presence of lipids. Since the lipid resonance is very close to the lactate resonance, lactate quantification is challenging. Moreover, lactate concentration can vary substantially in breast tissues due to natural causes such as lactation. As a result of these challenges, the key prognostic metabolite in MRS of breast is choline resonance at ~3.2 ppm (Cho). This resonance is comprised of several choline compounds including choline, phosphocholine, glycerophosphocholine, and taurine. While these metabolites can be spectrally resolved using high-resolution NMR spectroscopy, clinical MRI scanners do not have sufficient spectral resolution, and as a consequence, this resonance is frequently referred to as total Cho[72].

MRS techniques have progressed from a single-voxel spectroscopy technique to a multi-voxel chemical shift imaging (CSI) technique. In CSI, the spectra from multiple voxels are recorded simultaneously during MRS scan. For example, **Figure 8** shows a 2D CSI grid of 6×6 proton spectra of choline resonance, which have been recorded using localization over the breast. (Note that 3D CSI acquisitions are also feasible.) The Cho resonance intensity can be converted to mM concentration for each voxel in CSI and plotted as a metabolite map. The key strengths of CSI are the possibility of metabolite mapping and improvement in the voxel size compared to single-voxel spectroscopy. The resulting metabolite CSI maps can be overlaid over standard-of-care MRI scans. Moreover, the obtained Cho concentrations can be employed for diagnostic purpose.

MRS detection typically employs some variant of Point REsolved SpectoScopy (PRESS) pulse sequence, although some MRI scanners may employ Stimulated Echo Acquisition Mode (STEAM) or simple spin-echo acquisition schemes. The typical clinical MRS scan takes 5-15 minutes. A number of quantification approaches have been developed for converting the Cho signal into molar concentration. The method that gained popularity avoids the use of external calibration phantoms—instead, a corresponding data set is acquired without water signal suppression[72]. As the resulting water signal is substantially stronger than that of Cho, the corresponding water signal reference map can be recorded rapidly. In the next step, the signal of water is employed as a reference signal with known water concentration in breast tissue (ca. 91 M[73]) to obtain the molar Cho concentration. A number of correction factors are applied during quantification to account for the different T_1, T_2, number of protons contributing to the resonance

signal, and the number of scans/averages for Cho CSI and reference scan respectively. This method is insensitive to the variable sensitivity of breast proton MRS measurements. Moreover, the method does not require the use of external phantoms for quantification. This quantification approach has been successfully applied to a wide range of magnetic fields including clinically relevant 1.5 T[74].

The use of Cho resonance in proton MRS as a marker of malignancy has a reported sensitivity range of 71-74% and the specificity of 78-88%. These values are overall comparable to those of DWI MRI (84-91% and 75-84%, respectively[75]). Despite being a comparatively good diagnostic tool, MRS remains more a less a research tool, whereas DWI has enjoyed more widespread clinical adaptation because MRS of breast has the disadvantages of (i) relatively long acquisition times, (ii) frequent instances of exams with low quality spectra, (iii) challenging standardization[75].

6. Hyperpolarized [1-^{13}C]-Pyruvate

Conventional MRI forms images that reflect the spatial distribution of hydrogen atoms, subject to relaxation mechanisms that confer the outstanding soft-tissue contrast for which MRI is well known. Although the signal that is measured to generate images arises from only a small fraction of hydrogen nuclei (~10 parts per million at 3T), traditional ^{1}H MRI is feasible over a clinically practical timeframe because hydrogen is the most abundant atom in biological tissue, and the relative sensitivity to the hydrogen nucleus (a single proton) is the highest among stable atomic nuclei. MRI scanners can be tuned to be sensitive to other atomic nuclei, but these measurements face compounding barriers due to lower sensitivity and lower concentration that would be typically be overcome by signal averaging over impractically long acquisition times.

A number of methods have been proposed to overcome this barrier by enhancing the fraction of atomic nuclei that contribute signal to the imaging measurement. In recent years, dissolution dynamic nuclear polarization (dDNP) has been used to generate hyperpolarized (HP) ^{13}C-enriched imaging agents with nuclear polarization ranging from 20-50%, resulting in signal enhancement of four to five orders of magnitude[76, 77] that permits real-time spectroscopic imaging of key ^{13}C-enriched imaging agents and their metabolites. HP [1-^{13}C]-pyruvate is the most widely studied of these agents to date for a number of reasons. Pyruvate occupies an important metabolic branching point, it has favorable polarization characteristics, a relatively long T_1 relaxation time

constant, and rapid pharmacokinetics that allows insight into metabolic biochemistry within its observable signal lifetime. The spin label carried by the ^{13}C nucleus persists through chemical conversion, and the position of the spin label in the unique molecular environment of pyruvate and its metabolites (**Figure 9**) confers a unique chemical signature for each metabolite.

The conversion of HP pyruvate into lactate is of particular importance in oncology as aerobic glycolysis, the conversion of pyruvate to lactate in the presence of oxygen, is upregulated in many cancers. HP pyruvate is administered by intraveneous injection and is carried to the tumor through the vasculature. After extravasation, pyruvate enters cells primarily through monocarboxylate transporter 1 (MCT1). The chemical conversion of HP pyruvate to lactate in cytosol is mediated by the enzyme lactate dehydrogenase A (LDHA) and cofactor nicotinamide adenine dinucleotide (NADH). Molecules of HP [1-^{13}C]-pyruvate that enter the citric acid cycle lose the ^{13}C label to $^{13}CO_2$ in the first step of the pyruvate dehydrogenase complex, which converts pyruvate into acetyl coenzyme A. (HP bicarbonate is often observed following this reaction because bicarbonate is in rapid chemical equilibrium with CO_2). HP pyruvate can also be transaminated to form alanine.

Spectroscopy and spectroscopic imaging of the dynamic interaction between HP imaging agents and target biology is complicated by the fact that the enhanced spin polarization that is established in the polarizer is finite and non-renewable once removed from the polarizer, and continuously depleted by spin-lattice relaxation and signal excitations that are necessary for imaging. Imaging protocols must be optimized to balance the need for spatial encoding, spectral encoding, and sufficient time for interaction between the HP imaging agent and target biology. Since each signal excitation affects all future observations, the acquisition strategy must also be designed with careful consideration of the planned approach to signal analysis.

Signals from HP imaging agents are evanescent and change continuously over the course of their visible lifetime (**Figure 10**). Acquisition of dynamic HP MR images typically begins prior to arrival of the bolus injection, and signal is visible for only a few seconds to minutes after arrival. A variety of quantitative and semi-quantitative methods have been proposed to summarize dynamic HP MRI data[78, 79]. Pharmacokinetic (PK) models of signal evolution[80, 81] can be used to extract k_{PL}, the apparent rate constant for conversion of HP pyruvate into lactate, as an imaging biomarker for tumor metabolism. These models vary significantly in complexity, with more physiologically accurate PK models requiring a larger number of parameters that must be

determined by fitting model predictions to dynamic data during pharmacokinetic analysis. Simpler models with fewer parameters are easier to fit, but simplifying assumptions often lead to some ambiguity in the interpretation of parameter values. Studies are currently underway to determine the appropriate level of complexity and prior information that may be included to facilitate quantitative analysis for specific applications. The normalized lactate ratio (nLac), calculated as the area under the lactate curve divided by the sum of the areas under pyruvate and lactate curves, is a semi-quantitative biomarker that is often used to summarize the conversion of HP pyruvate into lactate. While nLac is appealing as the calculation is straightforward, it does not account for the perturbation of signal evolution imposed by the imaging sequence itself, and therefore comparison of nLac values between studies or acquired under different experimental conditions can be difficult.

There is tremendous potential for HP MRI to provide unique new information to improve our understanding of disease and response to therapy. Several preclinical studies have shown that conversion of HP pyruvate into lactate increases with tumor aggressiveness and can provide early indications of response to treatment[82]. The safety and feasibility of metabolic MRI using HP [1-^{13}C]-pyruvate in human studies has been proven[83], and this technology is now being evaluated in a number of clinical trials involving patients with cancers of the prostate, breast, brain, liver, pancreas, kidney, and other sites.

Recent studies have also demonstrated the safety and feasibility of HP MRI in patients with breast cancer. Gallagher *et al*. recently reported that lactate conversion significantly correlated with tumor volume and MCT1, and that conversion was observed to be higher in patients with more aggressive tumors[84]. Although this study enrolled a relatively modest number of participants, it suggests that this technology could address an unmet need for early indications of response to neoadjuvant therapy in aggressive breast tumors. A significant reduction in the HP lactate-to-pyruvate ratio was subsequently reported in a patient with aggressive triple-negative breast cancer following a single cycle of neoadjuvant chemotherapy[85]. The lower HP lactate-to-pyruvate ratio suggested that the tumor was responding to therapy, and that patient was later confirmed to have had a complete pathologic response. These studies are highly encouraging but remain somewhat limited by small sample sizes. Larger studies are needed to confirm these results and clarify the role that HP MRI may play in management of patients with breast cancer.

7. MRI-constrained radiomics and habitat imaging

Traditionally, a trained radiologist interprets the breast MRI and provides critical recommendations for the clinical management of a patient's disease; however, these assessments are subjective and variable between readers[86, 87]. The field of radiomics, defined as the conversion of medical images into mineable data, seeks to automate the derivation of insights from information-rich image data to aid in clinical decision making[88, 89]. Radiomics of breast MRI has demonstrated promise in advancing diagnostics[90-92], prognostics[93-96], and the prediction of therapeutic response[97-100]. Within radiomics studies, quantitative features from breast MRI are extracted and incorporated into machine learning models, enabling the integration of high-dimensional data to aid in the detection and diagnoses of breast cancer[101].

Figure 11 illustrates a typical radiomics workflow for breast MRI, which includes the following steps: 1) image acquisition and processing, 2) lesion localization and segmentation, 3) feature extraction, and 4) data analysis and model development. During a clinical MRI session, a variety of pulse sequences (e.g., DW-MRI, and pre- and post-contrast T_1-weighted MRI) may be used to acquire multiple images that provide varying contrast between different tissue structures. For downstream analyses, it is often necessary to ensure image alignment and correct for any patient motion during the acquisition via image registration across scans. The acquired data may then require additional processing, such as the generation of parametric maps (e.g., apparent diffusion coefficient maps from DW-MRI, Figure 11A) or image harmonization to standardize data acquired with different scanners or acquisition protocols[102-104]. After data acquisition and processing, the lesion is localized and segmented (Figure 11B). Segmentation of the tumor volume is traditionally accomplished manually, although this approach can be subjective and susceptible to inter-reader variability[105]. As lesion segmentation can significantly influence calculated features, automated segmentation techniques are of interest to improve repeatability and reproducibility of radiomics analyses[106]. A commonly implemented approach to automated segmentation of breast lesions was developed by Chen et al., who employed fuzzy C-means clustering of DCE-MRI to discriminate lesions from surrounding tissue[107]. With lesions segmented, quantitative features are then extracted (Figure 11C), describing a variety of tumor attributes, such as lesion shape (e.g., volume and surface area), enhancement kinetics (e.g., contrast wash-in rate), and parameter distributions (e.g., kurtosis and skew)[108]. These features are then integrated into machine learning models for a number of clinical applications, including

distinguishing benign versus malignant lesions[90-92], and identifying patients at higher risk of disease recurrence[109-111]. In the field of radiogenomics, investigators utilize machine learning techniques to link imaging features with biomolecular information[112]. Radiogenomics studies have found significant associations between breast cancer imaging and molecular phenotypes[113-115] and have utilized this information for the prediction of breast cancer subtype[116-118] as well as risk of disease recurrence[109, 119].

Radiomics features are often computed for the entire lesion, with an underlying assumption that heterogeneity within a tumor is "well-mixed"[120]. However, within clinical image data, intratumoral heterogeneity at the tissue level is observed as spatially-distinct subregions[121, 122], and analysis of tumor subregions has demonstrated improved diagnostic predictions compared to whole tumor analyses[123, 124]. Habitat imaging is a technique that characterizes intratumoral heterogeneity using multiparametric MRI data to spatially resolve tumor subregions or "habitats"[125]. Typically, after image registration and lesion segmentation, multiparametric voxel data of the tumor region are clustered to identify habitats (Figure 11B)[125]. Radiomics studies have then computed features from tumor habitats to incorporate breast tumor heterogeneity in model predictions of Ki-67 status[126], breast cancer subtype[127], and response to neoadjuvant therapy[128, 129]. For example, Wu et al. used DCE-MRI data acquired prior to the start of neoadjuvant therapy to identify habitats within breast tumors[130]. The investigators then used habitat features to stratify patients into two subgroups and, via these characterizations of pre-treatment tumor heterogeneity, found one subgroup was associated with increased risk of disease recurrence[130]. It is hypothesized that tumor habitats exert unique selection forces on the cell populations within them, and thus potentially offer a surrogate representation of the cellular diversity within a tumor[120]. To investigate this hypothesis, investigators have imaged tumors and leveraged corresponding histological data to explore the underlying biology of imaged habitats in preclinical models of breast cancer[131-133]. Applications of habitat imaging in the clinical setting could provide an opportunity to profile tumors based on intratumoral heterogeneity characteristics and enable improved understanding of an individual patient's tumor physiology.

While radiomics and habitat imaging demonstrate promise to advance breast MRI research, a number of challenges remain for the translation of these techniques to clinical practice. A primary barrier for the expansion of radiomics is standardizing the acquisition, processing, and analysis of large amounts of data that are necessary for the development of radiomic models[106, 134]. As

reproducibility and repeatability of computed features is essential to ensure model generalizability[103, 135-137], efforts from groups, such as the Quantitative Imaging Network (QIN) and Image Biomarker Standardisation Initiative (IBSI) are currently working to standardize image acquisition and feature calculations[138, 139]. Additionally, radiomics benefits from large sample sizes, which provides improved statistical power[88]. This necessitates the buildout of publicly-available databases for the storage and sharing of well-curated data that needed for radiomic model development[88, 106, 134].

8. MRI-constrained Mathematical Modeling

Mathematical modeling of cancer is the science of defining systems of equations and mathematical formulations that capture the driving biological mechanisms of tumorigenesis. These models are designed to predict the temporal and/or spatial dynamics of cancer *in vitro* or *in vivo*. With reliable mathematical formulations, one can represent and interpret complex cancer data in terms of solvable formulae and equations. Additionally, mathematical models can generate and test hypotheses as well as predictions of future dynamics, and therefore may ultimately guide clinical decision-making and treatment optimization[140]. Mathematical modeling of cancer has a rich history across various cancer types and scales[141-145]. More recently, imaging-informed, biophysical mathematical models have been developed featuring careful integration of patient-specific data and solved with robust numerical methods. There is growing evidence that these imaging-informed models can accurately predict the spatiotemporal dynamics of cancers of the kidney[146], brain[147-153], lung[154, 155], pancreas[156-159], prostate[160, 161], and breast[162-169].

Imaging data is a fundamental enabler of mathematical modeling development[170-173] and, in particular, MRI provide many measurements of tumor characteristics (see, for example, the above sections). Importantly, these measurements can be collected at the time of diagnosis and at multiple time points throughout treatment to track the growth and therapeutic response of tumors, which are specific to individual patients. Mathematical models of cancer can be initialized and calibrated using these spatial and temporally resolved patient-specific data, such that their resolution yields individualized tumor forecasts that can be further validated against actual patient-specific outcomes. Unlike “big data” methods, imaging-informed mechanism-based mathematical models can evaluate tumor growth or response to therapy on a patient-specific basis without having to first train/calibrate the model utilizing large population datasets[172]. This mechanism-based

strategy may also facilitate the testing of therapeutic regimens, where the model system serves as an *in silico* twin for each patient to optimize and personalize regimens[140, 169]. Therefore, the ability to parameterize models with patient-specific imaging data that are readily accessible is difficult to overstate.

Reaction-diffusion models are partial differential equations (PDEs) that provide a common framework for integrating quantitative MRI data within a mechanism-based description of tumor spatiotemporal dynamics[143, 153, 161, 166, 169-171, 174, 175]. For example, the following reaction-diffusion PDE represents the evolution of tumor cells, $N_{TC}(\bar{x},t)$, with respect to time, t, and spatial position, $\bar{x}$:

$$\frac{\partial N_{TC}(\bar{x},t)}{\partial t} = \overbrace{\nabla\cdot(D\nabla N_{TC}(\bar{x},t))}^{\text{Diffusion}} + \overbrace{(g(\bar{x},t) - d(\bar{x},t))N_{TC}(\bar{x},t))}^{\text{Reaction}}, \quad (1)$$

where the change in tumor cell number per time ($\partial N_{TC}(\bar{x},t)/\partial t$) is governed by diffusive and reactive terms. The diffusion term describes the random outward movement of the tumor cells with coefficient D, which may be defined as a constant under the assumption that tumor cell spread is isotropic. However, this tumor cell movement can also be governed by specific functions that relate tumor cell movement to specific host tissue anatomy[151, 152, 161, 165]. The reaction term encompasses the proliferation ($g(\bar{x},t)$) and death ($d(\bar{x},t)$) of tumor cells in time and space. Logistic growth is commonly used in mathematical models of cancer, but other formulations for proliferation can been employed (see [143] for a review of mathematical descriptions of proliferation in cancer). The tumor cell death function can describe various dynamics which can eliminate tumor cells, such as therapy[168], immune response[141], and/or modulation of proliferation due to mechanical forces and stresses[161, 176-178].

The parameters within Eq. (1) can be determined in a patient-specific manner by leveraging longitudinal MRI measurements of tumor features, such as ROI morphology and volume, tumor cellularity (from diffusion data), and the evolving distribution of therapeutics (from, for example, contrast enhanced data) throughout the tumor[153, 168]. During calibration, the model is initialized and repeatedly solved for varying values of the parameters, which are updated in each model run to provide an increasingly better match to the patient's MRI measurements at a target timepoint[152, 174, 178, 179]. Once the model is calibrated to the patient's data, it can be reinitialized at the calibration's endpoint and simulated further in time to yield a forecast of the future growth and therapeutic response of the patient's tumor. These predictions can be validated against additional

MRI measurements at a later time as well as clinical outcomes (e.g., pathological response status). **Figure 12** illustrates this process of calibration and validation of a reaction-diffusion cancer model using longitudinal MRI data.

Examples of the reaction-diffusion model utilized to model clinically relevant problems of breast cancer using MRI data span the prediction and assessment of neoadjuvant therapies[165-168] to surgical planning for breast conserving surgery[180, 181]. Using a similar model to Eq. (1), where drug distribution is approximated using DCE-MRI data collected prior to and during neoadjuvant therapy (Figure 12), has enabled patient-specific predictions of tumor response to chemotherapies for breast cancer[168]. MR images have also been utilized in a modeling system combining a reaction-diffusion model accounting for the biological processes of wound healing with tissue biomechanics for wound contraction[180, 181]. This modeling scheme is shown to predict, pre-operatively, the outcome shape of the breast after conserving surgery within clinically useful accuracy.

While the reaction-diffusion framework is a popular method for mathematical modeling studies, we note that this is just one of numerous modeling strategies that can be integrated with patient-specific MRI data[151, 178]. One recent example establishes a new way to assess breast tumors using a computational fluid dynamics model of blood flow and interstitial transport developed to be constrained by individual DW- and DCE-MRI data for breast cancer patients[182]. Using advanced image processing methods to generate tumor-related vasculature geometry, the mathematical model was used to characterize the tumor-associated blood supply unique to each patient, and significant differences were found between the modeling results for benign and malignant tumors.

8. Conclusion

It is clear that magnetic resonance imaging of the breast is in the process of moving far beyond merely providing high-contrast, anatomical images for morphological assessment. The field is now capable of offering quantitative insights into tumor biology at the physiological, cellular, and molecular levels. Furthermore, there are emerging methods that seek to summarize these data in ways that can provide more information than each data type individually. As these approaches mature and become more widely available, they will be incorporated into clinical trials

of interventions designed to induce changes in tumor biology that will be difficult to measure with standard, anatomical-based MRI.

9. Acknowledgements

We offer our sincere thank you to all the women who volunteer to participate in our studies; your strength and courage are examples for all of us. We thank the National Institutes of Health for funding through 5U01 CA142565 (TEY and GSK), 1U01 CA174706 (TEY), 1R01 CA186193 (TEY), 1R01 CA211150 (JAB), 1U24 CA226110 (TEY), R21CA220137 (EYC), 1R21HL154032, K25CA204599 (JAW). T.E.Y. is a CPRIT Scholar of Cancer Research *via* CPRIT RR160005. GL acknowledges funding from the European Union's Horizon 2020 research and innovation programme under the Marie Skłodowska-Curie grant agreement No. 838786.

References

1. Jansen, S.A., et al., Characterizing early contrast uptake of ductal carcinoma in situ with high temporal resolution dynamic contrast-enhanced MRI of the breast: a pilot study. Phys Med Biol, 2010. 55(19): p. N473-85.
2. Pineda, F.D., et al., Ultrafast Bilateral DCE-MRI of the Breast with Conventional Fourier Sampling: Preliminary Evaluation of Semi-quantitative Analysis. Acad Radiol, 2016. 23(9): p. 1137-44.
3. Milenkovic, J., et al., Textural analysis of early-phase spatiotemporal changes in contrast enhancement of breast lesions imaged with an ultrafast DCE-MRI protocol. Med Phys, 2017. 44(9): p. 4652-4664.
4. Platel, B., et al., Automated characterization of breast lesions imaged with an ultrafast DCE-MR protocol. IEEE Trans Med Imaging, 2014. 33(2): p. 225-32.
5. Woods, B.J., et al., Malignant-lesion segmentation using 4D co-occurrence texture analysis applied to dynamic contrast-enhanced magnetic resonance breast image data. J Magn Reson Imaging, 2007. 25(3): p. 495-501.
6. Agner, S.C., et al., Textural kinetics: a novel dynamic contrast-enhanced (DCE)-MRI feature for breast lesion classification. J Digit Imaging, 2011. 24(3): p. 446-63.
7. Henderson, E., B.K. Rutt, and T.Y. Lee, Temporal sampling requirements for the tracer kinetics modeling of breast disease. Magn Reson Imaging, 1998. 16(9): p. 1057-73.
8. Parker, G.J., et al., Experimentally-derived functional form for a population-averaged high-temporal-resolution arterial input function for dynamic contrast-enhanced MRI. Magn Reson Med, 2006. 56(5): p. 993-1000.
9. Yankeelov, T.E., et al., Comparison of a reference region model with direct measurement of an AIF in the analysis of DCE-MRI data. Magn Reson Med, 2007. 57(2): p. 353-61.
10. Kershaw, L.E. and H.L. Cheng, Temporal resolution and SNR requirements for accurate DCE-MRI data analysis using the AATH model. Magn Reson Med, 2010. 64(6): p. 1772-80.
11. Abe, H., et al., Kinetic Analysis of Benign and Malignant Breast Lesions With Ultrafast Dynamic Contrast-Enhanced MRI: Comparison With Standard Kinetic Assessment. AJR Am J Roentgenol, 2016: p. 1-8.

12. Pinker, K., et al., A combined high temporal and high spatial resolution 3 Tesla MR imaging protocol for the assessment of breast lesions: initial results. Invest Radiol, 2009. 44(9): p. 553-8.
13. Planey, C.R., et al., Temporal sampling requirements for reference region modeling of DCE-MRI data in human breast cancer. J Magn Reson Imaging, 2009. 30(1): p. 121-34.
14. Mus, R.D., et al., Time to enhancement derived from ultrafast breast MRI as a novel parameter to discriminate benign from malignant breast lesions. Eur J Radiol, 2017. 89: p. 90-96.
15. Vreemann, S., et al., Compressed Sensing for Breast MRI: Resolving the Trade-Off Between Spatial and Temporal Resolution. Invest Radiol, 2017. 52(10): p. 574-582.
16. Saranathan, M., et al., DIfferential Subsampling with Cartesian Ordering (DISCO): a high spatio-temporal resolution Dixon imaging sequence for multiphasic contrast enhanced abdominal imaging. J Magn Reson Imaging, 2012. 35(6): p. 1484-92.
17. Willinek, W.A., et al., 4D time-resolved MR angiography with keyhole (4D-TRAK): more than 60 times accelerated MRA using a combination of CENTRA, keyhole, and SENSE at 3.0T. J Magn Reson Imaging, 2008. 27(6): p. 1455-60.
18. Kershaw, L.E. and H.L. Cheng, A general dual-bolus approach for quantitative DCE-MRI. Magn Reson Imaging, 2011. 29(2): p. 160-6.
19. Korosec, F.R., et al., Time-resolved contrast-enhanced 3D MR angiography. Magn Reson Med, 1996. 36(3): p. 345-51.
20. Sartoretti, T., et al., Common artefacts encountered on images acquired with combined compressed sensing and SENSE. Insights Imaging, 2018. 9(6): p. 1107-1115.
21. Smith, D.S., et al., Quantitative effects of using compressed sensing in dynamic contrast enhanced MRI. Phys Med Biol, 2011. 56(15): p. 4933-46.
22. Wang, H., et al., Feasibility of high temporal resolution breast DCE-MRI using compressed sensing theory. Med Phys, 2010. 37(9): p. 4971-81.
23. Wang, Z., et al., Image quality assessment: from error visibility to structural similarity. IEEE Trans Image Process, 2004. 13(4): p. 600-12.
24. Yang, A.C., et al., Sparse Reconstruction Techniques in Magnetic Resonance Imaging: Methods, Applications, and Challenges to Clinical Adoption. Invest Radiol, 2016. 51(6): p. 349-64.

25. Hammernik, K., et al., Learning a variational network for reconstruction of accelerated MRI data. Magn Reson Med, 2018. 79(6): p. 3055-3071.
26. Yang, G., et al., DAGAN: Deep De-Aliasing Generative Adversarial Networks for Fast Compressed Sensing MRI Reconstruction. IEEE Trans Med Imaging, 2018. 37(6): p. 1310-1321.
27. Pineda, F., Medved, M., Fan, X., Karczmar, G. Unfolding of aliased dynamic acquisitions for the accelaration of breast dynamic contrast enhanced MRI (DCE-MRI). in American Association of Physicists in Medicine. 2016. Washington, D.C.
28. Pineda F, S.D., Medved M, Abe H, Karczmar G. Low-Dose Imaging Technique (LITE) MRI: Initial Experience in Breast Imaging. P. in 61st American Association of Physicists in Medine Annual Meeting. 2019. San Antonio, Texas.
29. Wu, C., et al., Quantitative analysis of vascular properties derived from ultrafast DCE-MRI to discriminate malignant and benign breast tumors. Magn Reson Med, 2019. 81(3): p. 2147-2160.
30. Patlak, C.S., R.G. Blasberg, and J.D. Fenstermacher, Graphical evaluation of blood-to-brain transfer constants from multiple-time uptake data. J Cereb Blood Flow Metab, 1983. 3(1): p. 1-7.
31. He, D., et al., A compact solution for estimation of physiological parameters from ultrafast prostate dynamic contrast enhanced MRI. Phys Med Biol, 2019. 64(15): p. 155012.
32. Wang, S., et al., Arterial input functions (AIFs) measured directly from arteries with low and standard doses of contrast agent, and AIFs derived from reference tissues. Magn Reson Imaging, 2016. 34(2): p. 197-203.
33. Wu C, Hormuth DA, Oliver TA, Pineda F, Lorenzo G, Karczmar GS, Moser RD, Yankeelov TE. Patient-Specific Characterization of Breast Cancer Hemodynamics Using Image-Guided Computational Fluid Dynamics. IEEE Trans Med Imaging. 2020 Sep;39(9):2760-2771.
34. DeFilippis RA, Chang H, Dumont N, et al. CD36 repression activates a multicellular stromal program shared by high mammographic density and tumor tissues. Cancer Discov. 2012;2(9):826-39.

35. Provenzano PP, Inman DR, Eliceiri KW, et al. Collagen density promotes mammary tumor initiation and progression. BMC Med. 2008;6:11.
36. Paszek MJ, Weaver VM. The tension mounts: mechanics meets morphogenesis and malignancy. J Mammary Gland Biol Neoplasia. 2004;9(4):325-42.
37. Huang S, Ingber DE. Cell tension, matrix mechanics, and cancer development. Cancer Cell. 2005;8(3):175-6.
38. Paszek MJ, Zahir N, Lakins JN, et al. Mechano-signaling in mammary morphogenesis and tumorigenesis. Mol Biol Cell. 2004;15:241a-a.
39. Samani A, Zubovits J, Plewes D. Elastic moduli of normal and pathological human breast tissues: an inversion-technique-based investigation of 169 samples. Phys Med Biol. 2007;52(6):1565-76.
40. Li J, Zormpas-Petridis K, Boult JKR, et al. Investigating the Contribution of Collagen to the Tumor Biomechanical Phenotype with Noninvasive Magnetic Resonance Elastography. Cancer Res. 2019;79(22):5874-83.
41. Tan L, McGarry MD, Van Houten EE, et al. Gradient-Based Optimization for Poroelastic and Viscoelastic MR Elastography. IEEE Trans Med Imaging. 2017;36(1):236-50.
42. Righetti R, Ophir J, Srinivasan S, Krouskop TA. The feasibility of using elastography for imaging the Poisson's ratio in porous media. Ultrasound Med Biol. 2004;30(2):215-28.
43. Righetti R, Srinivasan S, Kumar AT, Ophir J, Krouskop TA. Assessing image quality in effective Poisson's ratio elastography and poroelastography: I. Phys Med Biol. 2007;52(5):1303-20.
44. Fovargue D, Nordsletten D, Sinkus R. Stiffness reconstruction methods for MR elastography. NMR Biomed. 2018;31(10):e3935.
45. Haruoni AA, Hossain J, El Khouli R, et al. Strain-encoded breast MRI in phantom and ex vivo specimens with histological validation: preliminary results. Med Phys. 2012;39(12):7710-8.
46. Weis JA, Flint KM, Sanchez V, Yankeelov TE, Miga MI. Assessing the accuracy and reproducibility of modality independent elastography in a murine model of breast cancer. J Med Imaging (Bellingham). 2015;2(3):036001.

47. Balleyguier C, Lakhdar AB, Dunant A, Mathieu MC, Delaloge S, Sinkus R. Value of whole breast magnetic resonance elastography added to MRI for lesion characterization. NMR Biomed. 2018;31(1).
48. Hawley JR, Kalra P, Mo X, Raterman B, Yee LD, Kolipaka A. Quantification of breast stiffness using MR elastography at 3 Tesla with a soft sternal driver: A reproducibility study. J Magn Reson Imaging. 2017;45(5):1379-84.
49. Patel BK, Samreen N, Zhou Y, et al. MR Elastography of the Breast: Evolution of Technique, Case Examples, and Future Directions. Clin Breast Cancer. 2020.
50. Bohte AE, Nelissen JL, Runge JH, et al. Breast magnetic resonance elastography: a review of clinical work and future perspectives. NMR Biomed. 2018;31(10):e3932.
51. Wolff SD, Balaban RS. Magnetization transfer contrast (MTC) and tissue water proton relaxation in vivo. Magn Reson Med. 1989;10(1):135-44.
52. van Zijl PC, Zhou J, Mori N, Payen JF, Wilson D, Mori S. Mechanism of magnetization transfer during on-resonance water saturation. A new approach to detect mobile proteins, peptides, and lipids. Magn Reson Med. 2003;49(3):440-9.
53. Ward KM, Aletras AH, Balaban RS. A new class of contrast agents for MRI based on proton chemical exchange dependent saturation transfer (CEST). J Magn Reson. 2000;143(1):79-87.
54. Zhang S, Seiler S, Wang X, et al. CEST-Dixon for human breast lesion characterization at 3 T: A preliminary study. Magn Reson Med. 2018;80(3):895-903.
55. Heller SL, Moy L, Lavianlivi S, Moccaldi M, Kim S. Differentiation of malignant and benign breast lesions using magnetization transfer imaging and dynamic contrast-enhanced MRI. J Magn Reson Imaging. 2013;37(1):138-45.
56. Bonini RH, Zeotti D, Saraiva LA, et al. Magnetization transfer ratio as a predictor of malignancy in breast lesions: preliminary results. Magn Reson Med. 2008;59(5):1030-4.
57. Schmitt B, Zamecnik P, Zaiss M, et al. A new contrast in MR mammography by means of chemical exchange saturation transfer (CEST) imaging at 3 Tesla: preliminary results. Rofo. 2011;183(11):1030-6.
58. Song X, Airan RD, Arifin DR, et al. Label-free in vivo molecular imaging of underglycosylated mucin-1 expression in tumour cells. Nat Commun. 2015;6:6719.

59. Dula AN, Dewey BE, Arlinghaus LR, et al. Optimization of 7-T chemical exchange saturation transfer parameters for validation of glycosaminoglycan and amide proton transfer of fibroglandular breast tissue. Radiology. 2015;275(1):255-61.
60. Chan KW, Jiang L, Cheng M, et al. CEST-MRI detects metabolite levels altered by breast cancer cell aggressiveness and chemotherapy response. NMR Biomed. 2016;29(6):806-16.
61. Dula AN, Arlinghaus LR, Dortch RD, et al. Amide proton transfer imaging of the breast at 3 T: establishing reproducibility and possible feasibility assessing chemotherapy response. Magn Reson Med. 2013;70(1):216-24.
62. Klomp DW, Dula AN, Arlinghaus LR, et al. Amide proton transfer imaging of the human breast at 7T: development and reproducibility. NMR Biomed. 2013;26(10):1271-7.
63. Henkelman RM, Huang X, Xiang QS, Stanisz GJ, Swanson SD, Bronskill MJ. Quantitative interpretation of magnetization transfer. Magn Reson Med. 1993;29(6):759-66.
64. Balaban RS, Ceckler TL. Magnetization transfer contrast in magnetic resonance imaging. Magn Reson Q. 1992;8(2):116-37.
65. Graham SJ, Henkelman RM. Pulsed magnetization transfer imaging: evaluation of technique. Radiology. 1999;212(3):903-10.
66. Goffeney N, Bulte JW, Duyn J, Bryant LH, Jr., van Zijl PC. Sensitive NMR detection of cationic-polymer-based gene delivery systems using saturation transfer via proton exchange. J Am Chem Soc. 2001;123(35):8628-9.
67. Arlinghaus LR, Dortch RD, Whisenant JG, Kang H, Abramson RG, Yankeelov TE. Quantitative Magnetization Transfer Imaging of the Breast at 3.0 T: Reproducibility in Healthy Volunteers. Tomography. 2016;2(4):260-6.
68. Virostko J, Sorace AG, Wu C, et al. Magnetization Transfer MRI of Breast Cancer in the Community Setting: Reproducibility and Preliminary Results in Neoadjuvant Therapy. Tomography. 2019;5(1):44-52.
69. Ross B, Michaelis T. Clinical-applications of magnetic resonance spectroscopy. Magn Reson Q. 1994;10(4):191-247.
70. Soares DP, Law M. Magnetic resonance spectroscopy of the brain: review of metabolites and clinical applications. Clinical Radiology. 2009;64(1):12-21.

71. Faghihi R, Zeinali-Rafsanjani B, Mosleh-Shirazi M-A, et al. Magnetic Resonance Spectroscopy and its Clinical Applications: A Review. Journal of Medical Imaging and Radiation Sciences. 2017;48(3):233-53.
72. Bolan PJ, Meisamy S, Baker EH, et al. In vivo quantification of choline compounds in the breast with 1H MR spectroscopy. Magn Reson Med. 2003;50(6):1134-43.
73. Dorrius MD, Pijnappel RM, Jansen-van der Weide MC, et al. Determination of Choline Concentration in Breast Lesions: Quantitative Multivoxel Proton MR Spectroscopy as a Promising Noninvasive Assessment Tool to Exclude Benign Lesions. Radiology. 2011;259(3):695-703.
74. Baik H-M, Su M-Y, Yu H, Nalcioglu O, Mehta R. Quantification of Choline-containing Compounds in Malignant Breast Tumors by 1H MR Spectroscopy Using Water as an Internal Reference at 1.5 T. Magn Reson Mater Phy. 2006;19(2):96-104.
75. Sardanelli F, Carbonaro LA, Montemezzi S, Cavedon C, Trimboli RM. Clinical Breast MR Using MRS or DWI: Who Is the Winner? Frontiers in Oncology. 2016;6(217).
76. Ardenkjaer-Larsen JH, Fridlund B, Gram A, et al. Increase in signal-to-noise ratio of > 10,000 times in liquid-state NMR. Proceedings of the National Academy of Sciences of the United States of America. 2003;100(18):10158-63.
77. Ardenkjaer-Larsen JH, Leach AM, Clarke N, Urbahn J, Anderson D, Skloss TW. Dynamic nuclear polarization polarizer for sterile use intent. NMR in biomedicine. 2011;24(8):927-32.
78. Daniels CJ, McLean MA, Schulte RF, et al. A comparison of quantitative methods for clinical imaging with hyperpolarized (13)C-pyruvate. NMR in biomedicine. 2016;29(4):387-99.
79. Larson PEZ, Chen HY, Gordon JW, et al. Investigation of analysis methods for hyperpolarized 13C-pyruvate metabolic MRI in prostate cancer patients. NMR in biomedicine. 2018;31(11):e3997.
80. Walker CM, Gordon JW, Xu Z, et al. Slice profile effects on quantitative analysis of hyperpolarized pyruvate. NMR in biomedicine. 2020;33(10):e4373.
81. Bankson JA, Walker CM, Ramirez MS, et al. Kinetic modeling and constrained reconstruction of hyperpolarized [1-13C]-pyruvate offers improved metabolic imaging of tumors. Cancer Res. 2015;75(22):4708-17.

82. Kurhanewicz J, Vigneron DB, Ardenkjaer-Larsen JH, et al. Hyperpolarized (13)C MRI: Path to Clinical Translation in Oncology. Neoplasia. 2019;21(1):1-16.
83. Nelson SJ, Kurhanewicz J, Vigneron DB, et al. Metabolic imaging of patients with prostate cancer using hyperpolarized [1-13C]pyruvate. Science translational medicine. 2013;5(198):198ra08.
84. Gallagher FA, Woitek R, McLean MA, et al. Imaging breast cancer using hyperpolarized carbon-13 MRI. Proc Natl Acad Sci U S A. 2020;117(4):2092-8.
85. Woitek R, McLean MA, Gill AB, et al. Hyperpolarized (13)C MRI of Tumor Metabolism Demonstrates Early Metabolic Response to Neoadjuvant Chemotherapy in Breast Cancer. Radiol Imaging Cancer. 2020;2(4):e200017.
86. Saha A, Harowicz MR, Mazurowski MA. Breast cancer MRI radiomics: An overview of algorithmic features and impact of inter-reader variability in annotating tumors. Med Phys. 2018;45(7):3076-85.
87. Mussurakis S, Buckley DL, Coady AM, Turnbull LW, Horsman A. Observer variability in the interpretation of contrast enhanced MRI of the breast. Br J Radiol. 1996;69(827):1009-16.
88. Gillies RJ, Kinahan PE, Hricak H. Radiomics: Images Are More than Pictures, They Are Data. Radiology. 2016;278(2):563-77.
89. Aerts HJ. The Potential of Radiomic-Based Phenotyping in Precision Medicine: A Review. JAMA Oncol. 2016;2(12):1636-42.
90. Parekh VS, Jacobs MA. Integrated radiomic framework for breast cancer and tumor biology using advanced machine learning and multiparametric MRI. NPJ Breast Cancer. 2017;3:43.
91. Steinbruecker F, Meyer-Baese A, Plant C, Schlossbauer T, U M-B. Selection of Spatiotemporal Features in Breast MRI to Differentiate between Malignant and Benign Small Lesions Using Computer-Aided Diagnosis. Advances in Artificial Neural Systems. 2012;2012:1-8.
92. Antropova N, Abe H, Giger ML. Use of clinical MRI maximum intensity projections for improved breast lesion classification with deep convolutional neural networks. J Med Imaging (Bellingham). 2018;5(1):014503.

93. Loiselle C, Eby PR, Kim JN, et al. Preoperative MRI improves prediction of extensive occult axillary lymph node metastases in breast cancer patients with a positive sentinel lymph node biopsy. Acad Radiol. 2014;21(1):92-8.
94. Dong Y, Feng Q, Yang W, et al. Preoperative prediction of sentinel lymph node metastasis in breast cancer based on radiomics of T2-weighted fat-suppression and diffusion-weighted MRI. Eur Radiol. 2018;28(2):582-91.
95. Fan M, Li H, Wang S, Zheng B, Zhang J, Li L. Radiomic analysis reveals DCE-MRI features for prediction of molecular subtypes of breast cancer. PLoS One. 2017;12(2):e0171683.
96. Agner SC, Rosen MA, Englander S, et al. Computerized image analysis for identifying triple-negative breast cancers and differentiating them from other molecular subtypes of breast cancer on dynamic contrast-enhanced MR images: a feasibility study. Radiology. 2014;272(1):91-9.
97. Banerjee I, Malladi S, Lee D, et al. Assessing treatment response in triple-negative breast cancer from quantitative image analysis in perfusion magnetic resonance imaging. J Med Imaging (Bellingham). 2018;5(1):011008.
98. Granzier RWY, van Nijnatten TJA, Woodruff HC, Smidt ML, Lobbes MBI. Exploring breast cancer response prediction to neoadjuvant systemic therapy using MRI-based radiomics: A systematic review. Eur J Radiol. 2019;121:108736.
99. Liu Z, Li Z, Qu J, et al. Radiomics of Multiparametric MRI for Pretreatment Prediction of Pathologic Complete Response to Neoadjuvant Chemotherapy in Breast Cancer: A Multicenter Study. Clin Cancer Res. 2019;25(12):3538-47.
100. Teruel JR, Heldahl MG, Goa PE, et al. Dynamic contrast-enhanced MRI texture analysis for pretreatment prediction of clinical and pathological response to neoadjuvant chemotherapy in patients with locally advanced breast cancer. NMR Biomed. 2014;27(8):887-96.
101. Li H, Giger M. Artificial intelligence and interpretations in breast cancer imaging. *Artificial Intelligence in Medicine*: Elsevier; 2021. p. 291–308.
102. van Timmeren JE, Cester D, Tanadini-Lang S, Alkadhi H, Baessler B. Radiomics in medical imaging-"how-to" guide and critical reflection. Insights Imaging. 2020;11(1):91.

103. Saha A, Yu X, Sahoo D, Mazurowski MA. Effects of MRI scanner parameters on breast cancer radiomics. Expert Syst Appl. 2017;87:384-91.
104. Yankeelov TE, Pickens DR, Price RR. Quantitative MRI in Cancer. Boca Raton, FL: CRC Press, Taylor & Francis Group; 2012.
105. Granzier RWY, Verbakel NMH, Ibrahim A, et al. MRI-based radiomics in breast cancer: feature robustness with respect to inter-observer segmentation variability. Sci Rep. 2020;10(1):14163.
106. Bi WL, Hosny A, Schabath MB, et al. Artificial intelligence in cancer imaging: Clinical challenges and applications. CA Cancer J Clin. 2019;69(2):127-57.
107. Chen W, Giger ML, Bick U. A fuzzy c-means (FCM)-based approach for computerized segmentation of breast lesions in dynamic contrast-enhanced MR images. Acad Radiol. 2006;13(1):63-72.
108. Kumar V, Gu Y, Basu S, et al. Radiomics: the process and the challenges. Magn Reson Imaging. 2012;30(9):1234-48.
109. Li H, Zhu Y, Burnside ES, et al. MR Imaging Radiomics Signatures for Predicting the Risk of Breast Cancer Recurrence as Given by Research Versions of MammaPrint, Oncotype DX, and PAM50 Gene Assays. Radiology. 2016;281(2):382-91.
110. Drukker K, Li H, Antropova N, Edwards A, Papaioannou J, Giger ML. Most-enhancing tumor volume by MRI radiomics predicts recurrence-free survival "early on" in neoadjuvant treatment of breast cancer. Cancer Imaging. 2018;18(1):12.
111. Huang SY, Franc BL, Harnish RJ, et al. Exploration of PET and MRI radiomic features for decoding breast cancer phenotypes and prognosis. NPJ Breast Cancer. 2018;4:24.
112. Gevaert O. Radiogenomics. In: Li R, Xing L, Napel S, Rubin D, editors. Radiomics and Radiogenomics. 1st ed. Boca Raton, FL: CRC Press, Taylor & Francis Group; 2019. p. 369–85.
113. Zhu Y, Li H, Guo W, et al. Deciphering Genomic Underpinnings of Quantitative MRI-based Radiomic Phenotypes of Invasive Breast Carcinoma. Sci Rep. 2015;5:17787.
114. Yamamoto S, Maki DD, Korn RL, Kuo MD. Radiogenomic analysis of breast cancer using MRI: a preliminary study to define the landscape. AJR Am J Roentgenol. 2012;199(3):654-63.

115. Guo W, Li H, Zhu Y, et al. Prediction of clinical phenotypes in invasive breast carcinomas from the integration of radiomics and genomics data. J Med Imaging (Bellingham). 2015;2(4):041007.
116. Sutton EJ, Oh JH, Dashevsky BZ, et al. Breast cancer subtype intertumor heterogeneity: MRI-based features predict results of a genomic assay. J Magn Reson Imaging. 2015;42(5):1398-406.
117. Grimm LJ, Zhang J, Mazurowski MA. Computational approach to radiogenomics of breast cancer: Luminal A and luminal B molecular subtypes are associated with imaging features on routine breast MRI extracted using computer vision algorithms. J Magn Reson Imaging. 2015;42(4):902-7.
118. Li H, Zhu Y, Burnside ES, et al. Quantitative MRI radiomics in the prediction of molecular classifications of breast cancer subtypes in the TCGA/TCIA data set. NPJ Breast Cancer. 2016;2.
119. Woodard GA, Ray KM, Joe BN, Price ER. Qualitative Radiogenomics: Association between Oncotype DX Test Recurrence Score and BI-RADS Mammographic and Breast MR Imaging Features. Radiology. 2018;286(1):60-70.
120. Gatenby RA, Grove O, Gillies RJ. Quantitative imaging in cancer evolution and ecology. Radiology. 2013;269(1):8-15.
121. Méndez CA, Pizzorni Ferrarese F, Summers P, Petralia G, Menegaz G. DCE-MRI and DWI Integration for Breast Lesions Assessment and Heterogeneity Quantification. Int J Biomed Imaging. 2012;2012:676808.
122. O'Connor JPB. Cancer heterogeneity and imaging. Semin Cell Dev Biol. 2017;64:48-57.
123. Arponent O, Sudah M, Masarwah A, et al. Diffusion-Weighted Imaging in 3.0 Tesla Breast MRI: Diagnostic Performance and Tumor Characterization Using Small Subregions vs. Whole Tumor Regions of Interest. PLoS One. 2015;10(10):e0138702.
124. Lu H, Yin J. Texture Analysis of Breast DCE-MRI Based on Intratumoral Subregions for Predicting HER2 2+ Status. Front Oncol. 2020;10:543.
125. Jardim-Perassi B, Martinez G, Gillies R. Habitat imaging of tumor evolution by magnetic resonance imaging (MRI). In: Li R, Xing L, Napel S, Rubin D, editors. Radiomics and Radiogenomics. Boca Raton, FL: CRC Press, Taylor & Francis Group; 2019. p. 115–20.

126. Fan M, Cheng H, Zhang P, et al. DCE-MRI texture analysis with tumor subregion partitioning for predicting Ki-67 status of estrogen receptor-positive breast cancers. J Magn Reson Imaging. 2018;48(1):237-47.
127. Chang RF, Chen HH, Chang YC, Huang CS, Chen JH, Lo CM. Quantification of breast tumor heterogeneity for ER status, HER2 status, and TN molecular subtype evaluation on DCE-MRI. Magn Reson Imaging. 2016;34(6):809-19.
128. Wu J, Gong G, Cui Y, Li R. Intratumor partitioning and texture analysis of dynamic contrast-enhanced (DCE)-MRI identifies relevant tumor subregions to predict pathological response of breast cancer to neoadjuvant chemotherapy. J Magn Reson Imaging. 2016;44(5):1107-15.
129. Braman NM, Etesami M, Prasanna P, et al. Intratumoral and peritumoral radiomics for the pretreatment prediction of pathological complete response to neoadjuvant chemotherapy based on breast DCE-MRI. Breast Cancer Res. 2017;19(1):57.
130. Wu J, Cao G, Sun X, et al. Intratumoral Spatial Heterogeneity at Perfusion MR Imaging Predicts Recurrence-free Survival in Locally Advanced Breast Cancer Treated with Neoadjuvant Chemotherapy. Radiology. 2018;288(1):26-35.
131. Schmitz J, Schwab J, Schwenck J, et al. Decoding Intratumoral Heterogeneity of Breast Cancer by Multiparametric In Vivo Imaging: A Translational Study. Cancer Res. 2016;76(18):5512-22.
132. Jardim-Perassi BV, Huang S, Dominguez-Viqueira W, et al. Multiparametric MRI and Coregistered Histology Identify Tumor Habitats in Breast Cancer Mouse Models. Cancer Res. 2019;79(15):3952-64.
133. Syed AK, Whisenant JG, Barnes SL, Sorace AG, Yankeelov TE. Multiparametric Analysis of Longitudinal Quantitative MRI data to Identify Distinct Tumor Habitats in Preclinical Models of Breast Cancer. Cancers (Basel). 2020;12(6).
134. Sala E, Mema E, Himoto Y, et al. Unravelling tumour heterogeneity using next-generation imaging: radiomics, radiogenomics, and habitat imaging. Clin Radiol. 2017;72(1):3-10.
135. Traverso A, Wee L, Dekker A, Gillies R. Repeatability and Reproducibility of Radiomic Features: A Systematic Review. Int J Radiat Oncol Biol Phys. 2018;102(4):1143-58.
136. Welch ML, McIntosh C, Haibe-Kains B, et al. Vulnerabilities of radiomic signature development: The need for safeguards. Radiother Oncol. 2019;130:2-9.

137. Cattell R, Chen S, Huang C. Robustness of radiomic features in magnetic resonance imaging: review and a phantom study. Vis Comput Ind Biomed Art. 2019;2(1):19.
138. Zwanenburg A, Vallières M, Abdalah MA, et al. The Image Biomarker Standardization Initiative: Standardized Quantitative Radiomics for High-Throughput Image-based Phenotyping. Radiology. 2020;295(2):328-38.
139. McNitt-Gray M, Napel S, Jaggi A, et al. Standardization in Quantitative Imaging: A Multicenter Comparison of Radiomic Features from Different Software Packages on Digital Reference Objects and Patient Data Sets. Tomography. 2020;6(2):118-28.
140. Jarrett AM, Faghihi D, Hormuth II DA, et al. Optimal Control Theory for Personalized Therapeutic Regimens in Oncology: Background, History, Challenges, and Opportunities. Journal of Clinical Medicine. 2020;9(1314).
141. Walker R, Enderling H. From concept to clinic: Mathematically informed immunotherapy. Curr Probl Cancer. 2016;40(1):68-83.
142. Yin AY, Moes D, van Hasselt JGC, Swen JJ, Guchelaar HJ. A Review of Mathematical Models for Tumor Dynamics and Treatment Resistance Evolution of Solid Tumors. Cpt-Pharmacometrics & Systems Pharmacology. 2019;8(10):720-37.
143. Jarrett AM, Lima EABF, Hormuth II DA, et al. Mathematical models of tumor cell proliferation: A review of the literature. Expert Review of Anticancer Therapy. 2018;18(12):1271-86.
144. Altrock PM, Liu LL, Michor F. The mathematics of cancer: integrating quantitative models. Nature Reviews Cancer. 2015;15(12):730-45.
145. Karolak A, Markov DA, McCawley LJ, Rejniak KA. Towards personalized computational oncology: from spatial models of tumour spheroids, to organoids, to tissues. J R Soc Interface. 2018;15(138).
146. Chen X, Summers RM, Yao J. Kidney tumor growth prediction by coupling reaction-diffusion and biomechanical model. IEEE Trans Biomed Eng. 2013;60(1):169-73.
147. Yuan J, Liu L. Brain glioma growth model using reaction-diffusion equation with viscous stress tensor on brain MR images. Magnetic Resonance Imaging. 2016;34 (2):114-9.
148. Rockne R, Rockhill JK, Mrugala M, et al. Predicting the efficacy of radiotherapy in individual glioblastoma patients in vivo: a mathematical modeling approach. Phys Med Biol. 2010;55(12):3271-85.

149. Clatz O, Sermesant M, Bondiau PY, et al. Realistic simulation of the 3-D growth of brain tumors in MR images coupling diffusion with biomechanical deformation. IEEE Transactions on Medical Imaging. 2005;24(10):1334-46.
150. Baldock AL, Rockne RC, Boone AD, et al. From patient-specific mathematical neuro-oncology to precision medicine. Front Oncol. 2013;3:62.
151. Agosti A, Giverso C, Faggiano E, Stamm A, Ciarletta P. A personalized mathematical tool for neuro-oncology: A clinical case study. International Journal of Non-Linear Mechanics. 2018;107:170-81
152. Mang A, Bakas S, Subramanian S, Davatzikos C, Biros G. Integrated Biophysical Modeling and Image Analysis: Application to Neuro-Oncology. Annu Rev Biomed Eng. 2020;22:309-41.
153. Hormuth II DA, Jarrett AM, Yankeelov TE. Forecasting tumor and vasculature response dynamics to radiation therapy via image based mathematical modeling. Radiat Oncol. 2020;15(1):4.
154. Mi H, Petitjean C, Dubray B, Vera P, Ruan S. Prediction of lung tumor evolution during radiotherapy in individual patients with PET. IEEE Trans Med Imaging. 2014;33(4):995-1003.
155. Mi H, Petitjean C, Vera P, Ruan S. Joint tumor growth prediction and tumor segmentation on therapeutic follow-up PET images. Med Image Anal. 2015;23(1):84-91.
156. Liu YX, Sadowski SM, Weisbrod AB, Kebebew E, Summers RM, Yao JH. Patient specific tumor growth prediction using multimodal images. Medical Image Analysis. 2014;18(3):555-66.
157. Wong KC, Summers RM, Kebebew E, Yao J. Pancreatic Tumor Growth Prediction With Elastic-Growth Decomposition, Image-Derived Motion, and FDM-FEM Coupling. IEEE Trans Med Imaging. 2017;36(1):111-23.
158. Liu Y, Sadowski SM, Weisbrod AB, Kebebew E, Summers RM, Yao J. Multimodal image driven patient specific tumor growth modeling. Med Image Comput Comput Assist Interv. 2013;16(Pt 3):283-90.
159. Wong KC, Summers RM, Kebebew E, Yao J. Tumor growth prediction with reaction-diffusion and hyperelastic biomechanical model by physiological data fusion. Med Image Anal. 2015;25(1):72-85.

160. Lorenzo G, Scott MA, Tew K, et al. Tissue-scale, personalized modeling and simulation of prostate cancer growth. Proc Natl Acad Sci U S A. 2016;113(48):E7663-E71.
161. Lorenzo G, Hughes TJR, Dominguez-Frojan P, Reali A, Gomez H. Computer simulations suggest that prostate enlargement due to benign prostatic hyperplasia mechanically impedes prostate cancer growth. Proc Natl Acad Sci U S A. 2019;116(4):1152-61.
162. Atuegwu NC, Colvin DC, Loveless ME, Xu L, Gore JC, Yankeelov TE. Incorporation of diffusion-weighted magnetic resonance imaging data into a simple mathematical model of tumor growth. Physics in Medicine and Biology. 2012;57(1):225-40.
163. Atuegwu NC, Gore JC, Yankeelov TE. The integration of quantitative multi-modality imaging data into mathematical models of tumors. Phys Med Biol. 2010;55(9):2429-49.
164. Atuegwu NC, Arlinghaus LR, Li X, et al. Parameterizing the Logistic Model of Tumor Growth by DW-MRI and DCE-MRI Data to Predict Treatment Response and Changes in Breast Cancer Cellularity during Neoadjuvant Chemotherapy. Translational Oncology. 2013;6(3):256-64.
165. Weis JA, Miga MI, Arlinghaus LR, et al. A mechanically coupled reaction-diffusion model for predicting the response of breast tumors to neoadjuvant chemotherapy. Physics in Medicine and Biology. 2013;58(17):5851-66.
166. Weis JA, Miga MI, Arlinghaus LR, et al. Predicting the Response of Breast Cancer to Neoadjuvant Therapy Using a Mechanically Coupled Reaction-Diffusion Model. Cancer Research. 2015;75(22):4697-707.
167. Weis JA, Miga MI, Yankeelov TE. Three-dimensional image-based mechanical modeling for predicting the response of breast cancer to neoadjuvant therapy. Computer Methods in Applied Mechanics and Engineering. 2017;314:494-512.
168. Jarrett AM, Hormuth II DA, Barnes SL, Feng X, Huang W, Yankeelov TE. Incorporating drug delivery into an imaging-driven, mechanics-coupled reaction diffusion model for predicting the response of breast cancer to neoadjuvant chemotherapy: theory and preliminary clinical results. Phys Med Biol. 2018;63(10):105015.
169. Jarrett AM, Hormuth II DA, Wu C, et al. Evaluating patient-specific neoadjuvant regimens for breast cancer v*ia* a mathematical model constrained by quantitative magnetic resonance imaging data. Neoplasia: Elsevier; 2020. p. 820-30.

170. Yankeelov TE, Quaranta V, Evans KJ, Rericha EC. Toward a Science of Tumor Forecasting for Clinical Oncology. Cancer Research. 2015;75(6):918-23.
171. Yankeelov TE, Atuegwu N, Hormuth II DA, et al. Clinically Relevant Modeling of Tumor Growth and Treatment Response. Science Translational Medicine. 2013;5(187).
172. Rockne RC, Hawkins-Daarud A, Swanson KR, et al. The 2019 mathematical oncology roadmap. Phys Biol. 2019;16(4):041005.
173. Alfonso JCL, Talkenberger K, Seifert M, et al. The biology and mathematical modelling of glioma invasion: a review. J R Soc Interface. 2017;14(136).
174. Hogea C, Davatzikos C, Biros G. An image-driven parameter estimation problem for a reaction-diffusion glioma growth model with mass effects. J Math Biol. 2008;56(6):793-825.
175. Hormuth II DA, Jarrett AM, Lima EABF, McKenna MT, Fuentes DT, Yankeelov TE. Mechanism-based Modeling of Tumor Growth and Treatment Response Constrained by Multiparametric Imaging Data. Jco Clinical Cancer Informatics. 2019(3):10.
176. Stylianopoulos T, Martin JD, Snuderl M, Mpekris F, Jain SR, Jain RK. Coevolution of solid stress and interstitial fluid pressure in tumors during progression: implications for vascular collapse. Cancer Res. 2013;73(13):3833-41.
177. Jain RK, Martin JD, Stylianopoulos T. The role of mechanical forces in tumor growth and therapy. Annu Rev Biomed Eng. 2014;16:321-46.
178. Lima EABF, Oden JT, Wohlmuth B, et al. Selection and validation of predictive models of radiation effects on tumor growth based on noninvasive imaging data. Computer Methods in Applied Mechanics and Engineering. 2017;327:277-305.
179. Hormuth II DA, Eldridge SL, Weis JA, Miga MI, Yankeelov TE. Mechanically Coupled Reaction-Diffusion Model to Predict Glioma Growth: Methodological Details. Methods Mol Biol. 2018;1711:225-41.
180. Vavourakis V, Eiben B, Hipwell JH, Williams NR, Keshtgar M, Hawkes DJ. Multiscale Mechano-Biological Finite Element Modelling of Oncoplastic Breast Surgery-Numerical Study towards Surgical Planning and Cosmetic Outcome Prediction. PLoS One. 2016;11(7):e0159766.
181. Eiben B, Breast Conserving Surgery Outcome Prediction: A Patient-Specific, Integrated Multi-modal Imaging and Mechano-Biological Modelling Framework In: A. T, K. L, P. T,

editors. Breast Imaging IWDM 2016 Lecture Notes in Computer Science. 9699: Springer; 2016.

182. Wu C, Hormuth II DA, Oliver TA, et al. Patient-Specific Characterization of Breast Cancer Hemodynamics Using Image-Guided Computational Fluid Dynamics. IEEE Trans Med Imaging. 2020;39(9):2760-71.

Figure Captions

Figure 1. Panel A presents a standard DCE-MRI acquisition with temporal resolution of 60 – 90 seconds per image. Panel B shows an ultrafast acquisition (in red), for approximately 30 seconds before and 45 seconds after contrast injection, integrated with standard acquisitions in blue before injection and during contrast media washout.

Figure 2. A cartoon depiction of a bolus of contrast agent traversing the vascular support of a lesion. Ultra-fast MRI is potentially capable of resolving the very different features of the arterial phase, lesion response, and venous output components of these dynamics. This information is simply not accessible at the temporal resolutions employed during standard-of-care MRI.

Figure 3. Quasi-static MR elastography of a breast tumor. Anatomical MR images before (left) and after (middle) external application of tissue deformation are used with a computational biomechanics model to estimate tissue mechanical elasticity properties (right).

Figure 4. Two-pool models for magnetization transfer and chemical exchange saturation transfer. Panel (A) presents a two-pool model of magnetization transfer where M_0^F and M_0^B represent the fully relaxed values of magnetization associated with the free and the bound pools, respectively. Each pool is characterized by its own longitudinal relaxation rate (R_F and R_B) and by its rate of loss of longitudinal magnetization due to the RF irradiation (R_{RFF} and R_{RFB}). The exchange rate between the two pools, R, is assumed to be symmetrical. The shaded portion of the boxes represents the spins in each pool that are saturated, while the white area represents the spins that are in the longitudinal plane, for a given instant of time. Panel (B) presents the two-pool model of CEST contrast enhancement illustrated with exchange between a solute pool and a solvent pool (water).

Figure 5. Magnetization transfer data acquisition. Panel (A) depicts a typical continuous wave MT-MRI pulse sequence for breast where the saturation pulse is typically a long (~ 9 ms) Gaussian pulse. Panel (B) displays an example of the MT pulse where $\Delta\omega$ is several hundred to several thousand Hertz away from the “free” water frequency to saturate the “bound” pool.

Figure 6. Chemical exchange saturation transfer data acquisition. Panel (A) shows a diagram of a pulsed-CEST imaging sequence where the irradiation train consists of a series of Gaussian pulses with flip angle θ (a multiple of 90° or 180°) and duration τ_p followed by interpulse delay τ_d, where $\tau_p + \tau_d$ is the duty cycle. These pulses are applied at a resonance frequency, $\Delta\omega$, at a saturation amplitude, B_1, and a total duration for the pulsed train t_{sat}. Panel (B) shows the application of saturation at $\pm \Delta\omega$ and the resulting signal intensity reduction due to MT, direct saturation (spillover), and the CEST effect.

Figure 7. Examples of CEST and MT MRI measurements in the human breast. Panel (A) displays MT-MRI performed before (left) and after (right) one cycle of chemotherapy suggests declines in MTR may correlate with therapeutic response. Panel (B) CEST-MRI measurements of amide proton transfer (APT) in the breast in a healthy subject (left) and an APT map of a breast with tumor indicated by an arrow (right).

Figure 8. Panel a presents a volume of interest (36 voxels of 0.25 cm 3 each) overlain on a transverse proton MRI centered on an invasive ductal carcinoma. Panel b displays a spectral map with intense water and minor fat peaks in the lesion. After application of water and fat suppression, Panel c presents the Cho peak in the tumor, as shown on spectra, and Panel d shows the Cho peak as hyperintense. Cr = creatine. (Reproduced with permission from X.)

Figure 9. Chemical endpoints of hyperpolarized [1-13C]-pyruvate *in vivo*. The molecular environment of the 13C label (left) imparts unique spectral offsets for pyruvate and its metabolites (right). The unlabeled peak represents pyruvate hydrate, which is not metabolically active.

Figure 10. Representative evolution of signal from hyperpolarized [1-13C]-pyruvate and its metabolites *in vivo*. After injection, HP pyruvate interacts with intracellular enzymes and the transfer of the spin label into different chemical pools can be quantified by dynamic MR spectroscopy or spectroscopic imaging.

Figure 11. The typical radiomics workflow with breast MRI and its use for clinical decision support. First, MRI data is acquired and processed (panel A) to, for example, correct for any patient motion or generate parametric maps. The lesion is then localized, and segmented (panel B) through manual or automated techniques to isolate the tumor region of interest (ROI). To spatially resolve intratumoral heterogeneity, additional subregions, or "habitats", within the tumor ROI can be identified. Finally, quantitative features (panel C) are extracted from the ROIs and may be combined with other modalities of information, such as genomic or clinical data. These features are ultimately integrated into models that can aid in clinical decision making for breast cancer patients, including diagnosis, prognosis, or prediction of therapeutic response (panel C).

Figure 12. Schematic of the tumor features extracted from MRI data to be incorporated into a reaction-diffusion mathematical model for calibration and prediction of tumor response to therapy on an individual patient basis. Panels (a) and (b) depict example DW- and DCE-MRI data, respectively, that are used to derive maps of the apparent diffusion coefficient (ADC) of water (panel (c)), tumor ROIs (panel (d), and physiological parameters describing the tumor associated vasculature (panel (e)). These imaging maps can then be used to calculate approximate tumor cellularity (panel (f)) and drug distribution (panel (g)) within the tumor to initialize and constrain variables and parameters within a reaction-diffusion mathematical model (panel (h)). With MRI scans acquired (for example) prior to therapy, during therapy, and after the completion of therapy (scans 1, 2, and 3 in panel (i), respectively), the model can be calibrated with early therapy data, and the resulting patient-specific parameter maps can be used to simulate the model forward in time to predict tumor response at the completion of the regimen. The final scan may be used to then evaluate the predictive ability of the model—comparing measured tumor response to the model forecast for each patient.

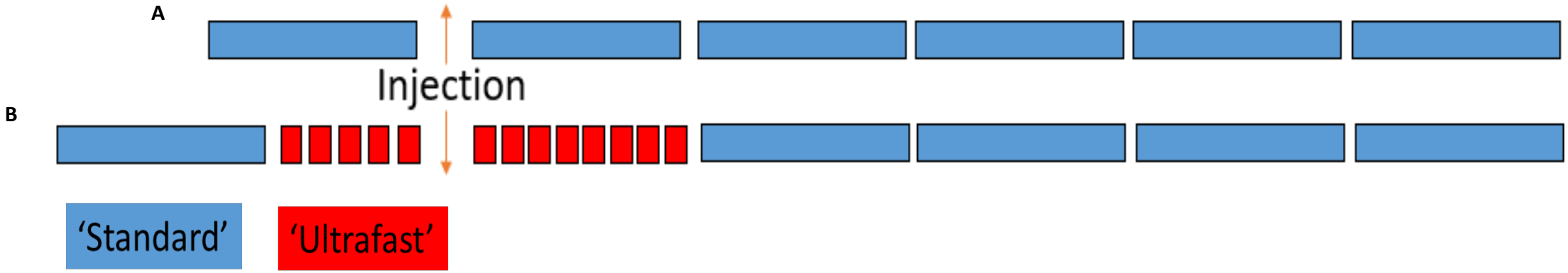
A
Injection
B
'Standard'
'Ultrafast'

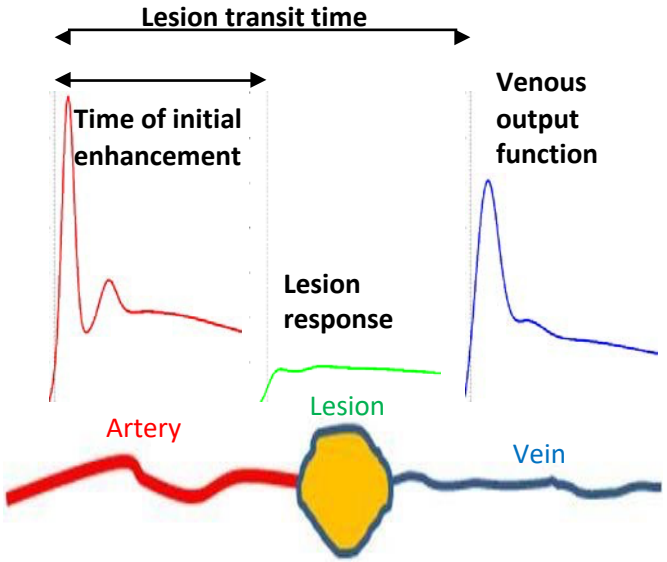
Lesion transit time
Time of initial enhancement
Venous output function
Lesion response
Lesion
Artery
Vein

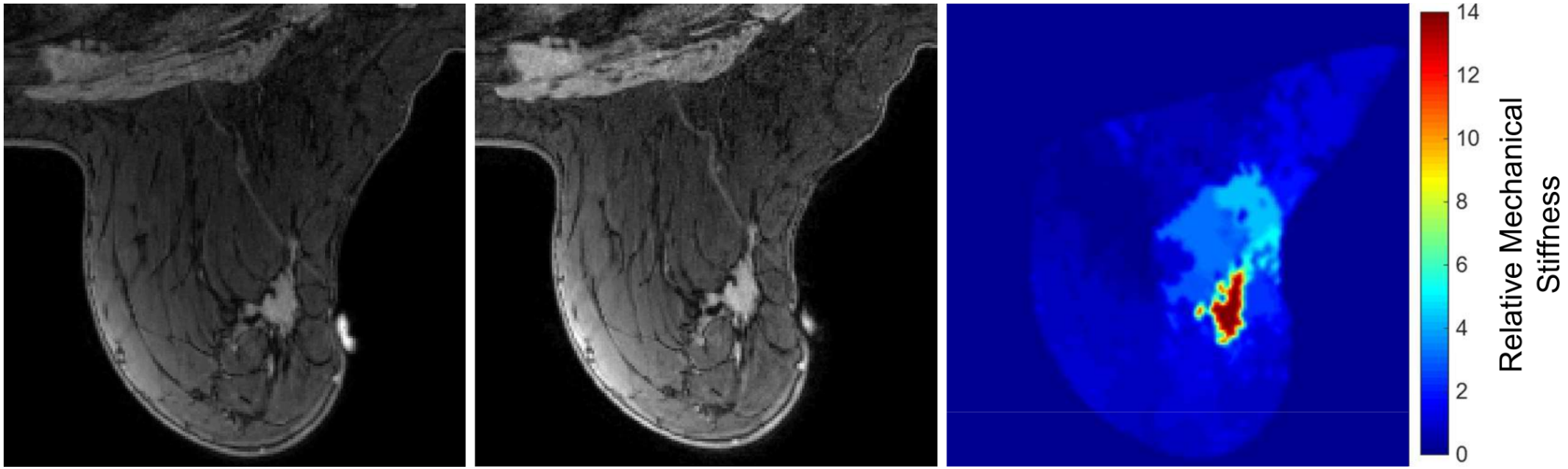
14
12
10
8
6
4
2
0
Relative Mechanical Stiffness

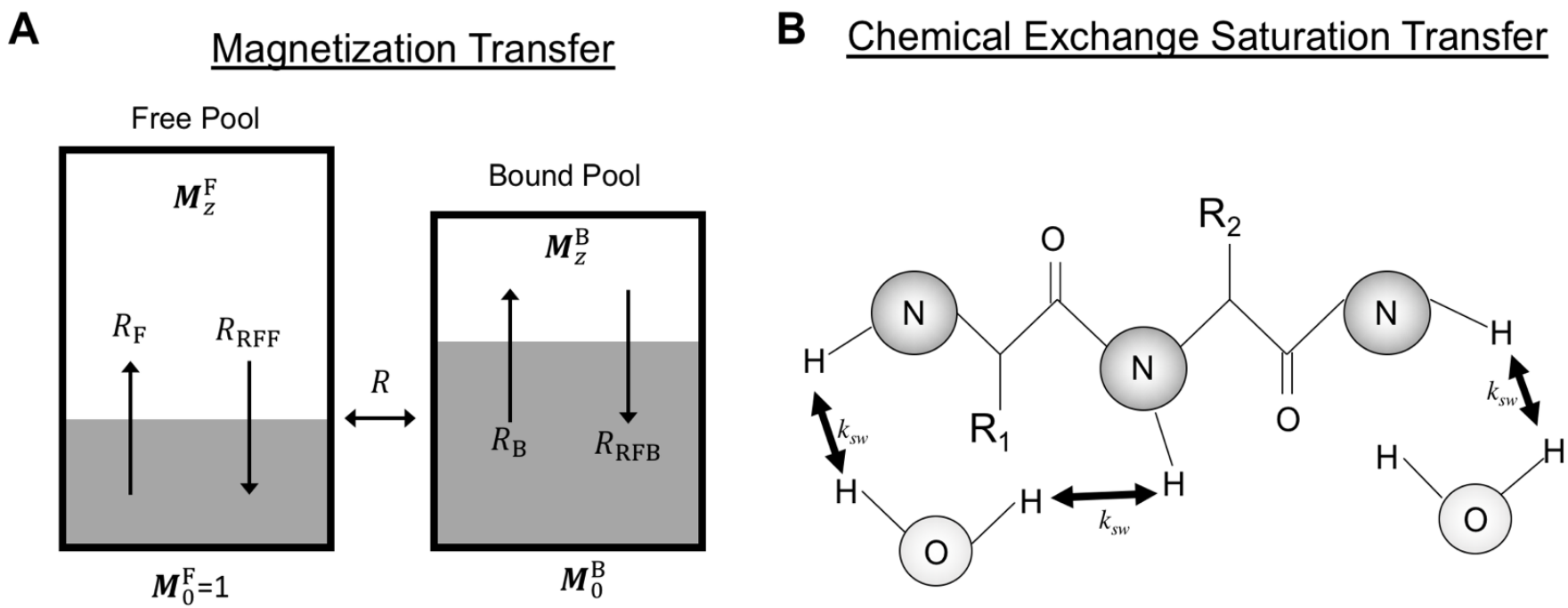
A
Magnetization Transfer
Free Pool
Bound Pool
M_z^F
M_z^B
R_F
R_{RFF}
R
R_B
R_{RFB}
M_0^F=1
M_0^B
B
Chemical Exchange Saturation Transfer
O
R_2
N
N
N
H
H
H
H
H
H
R_1
k_{sw}
k_{sw}
k_{sw}
O
O

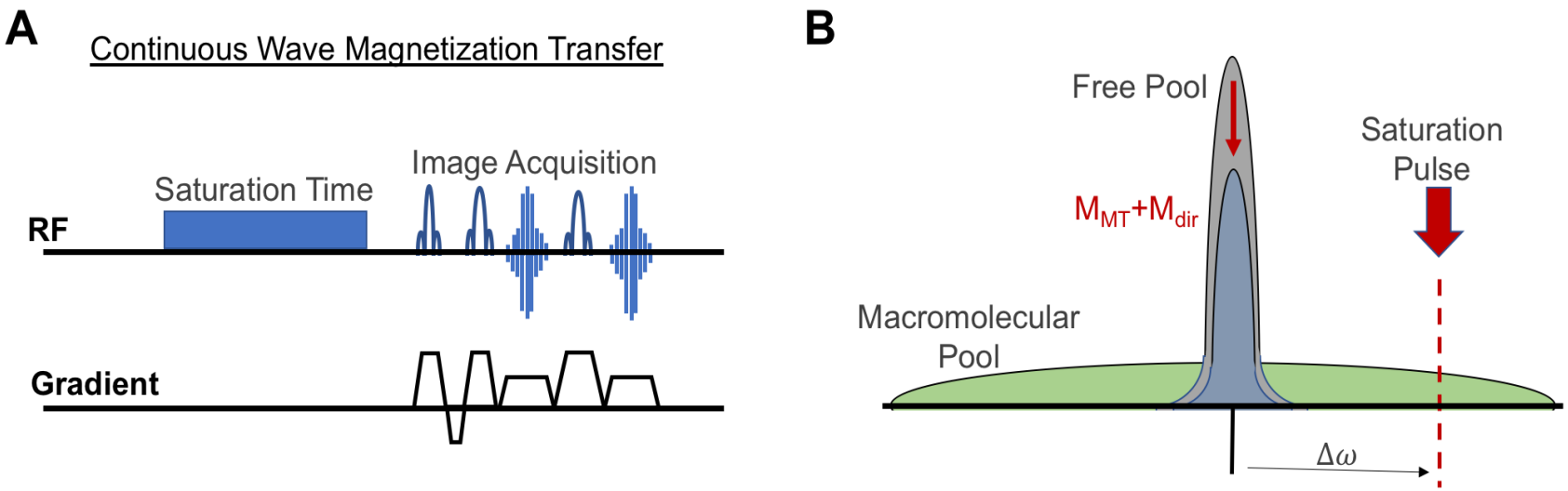
A
Continuous Wave Magnetization Transfer
Saturation Time
Image Acquisition
RF
Gradient
B
Free Pool
Saturation
Pulse
$M_{MT}+M_{dir}$
Macromolecular
Pool
$\Delta\omega$

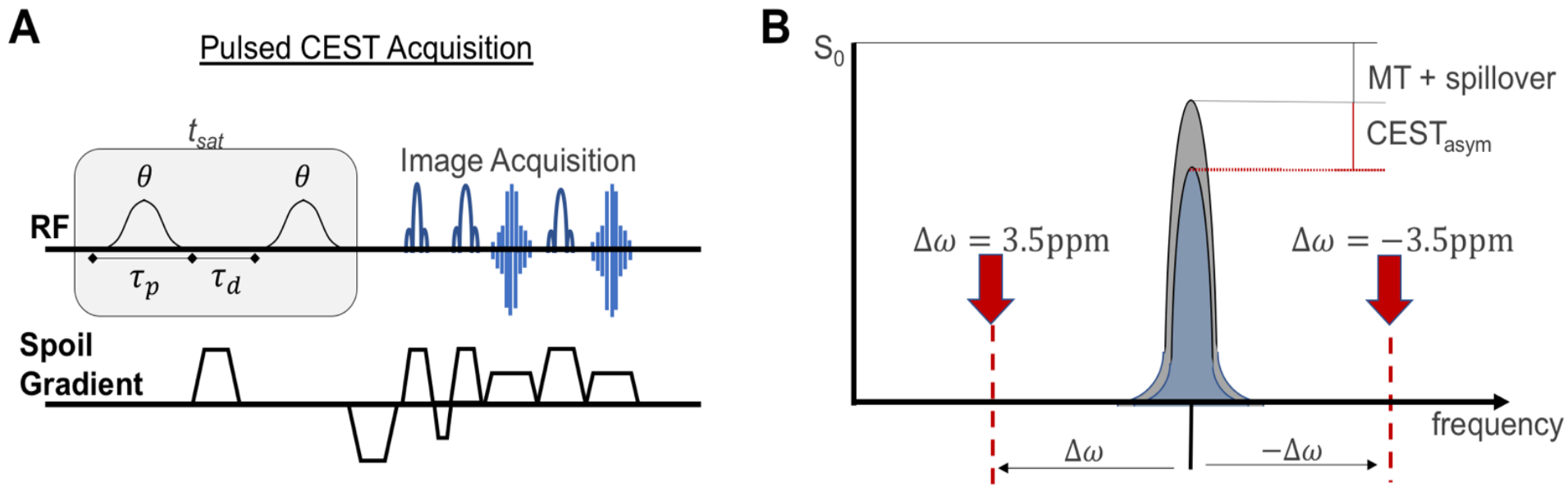
A
Pulsed CEST Acquisition
t_{sat}
θ
θ
RF
τ_p
τ_d
Image Acquisition
Spoil
Gradient
B
S_0
MT + spillover
$CEST_{asym}$
$\Delta\omega = 3.5$ppm
$\Delta\omega = -3.5$ppm
frequency
$\Delta\omega$
$-\Delta\omega$

A

MT-MRI in Patient with Complete Response

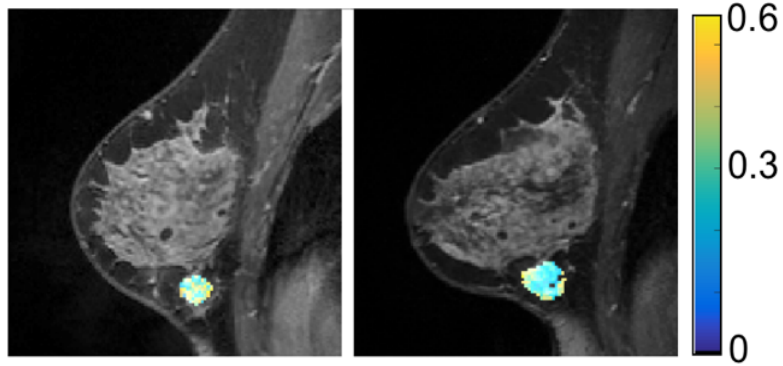

B

z-spectrum from Healthy Breast

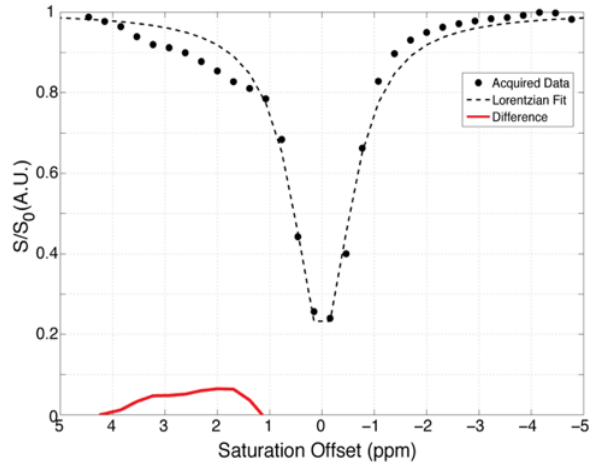

APT Map from CEST-MRI

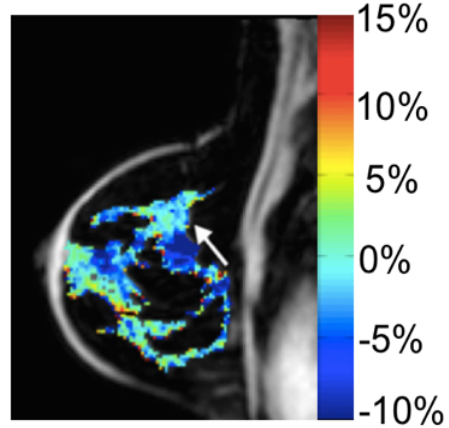

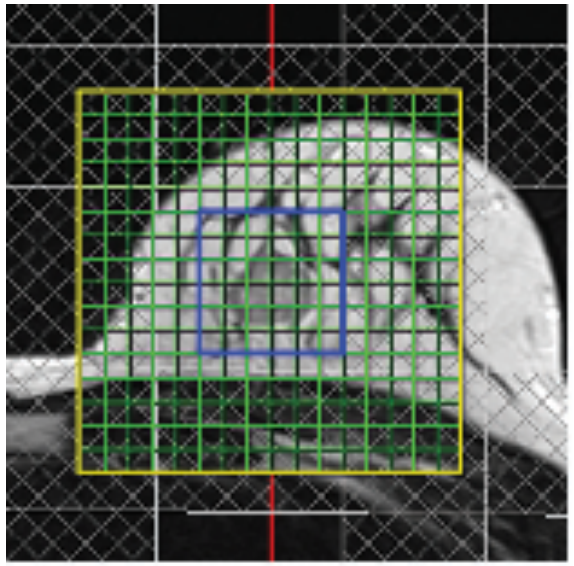

a.

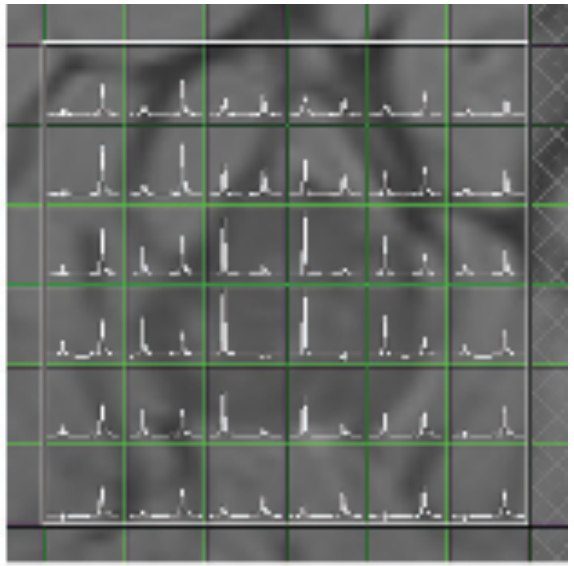

b.

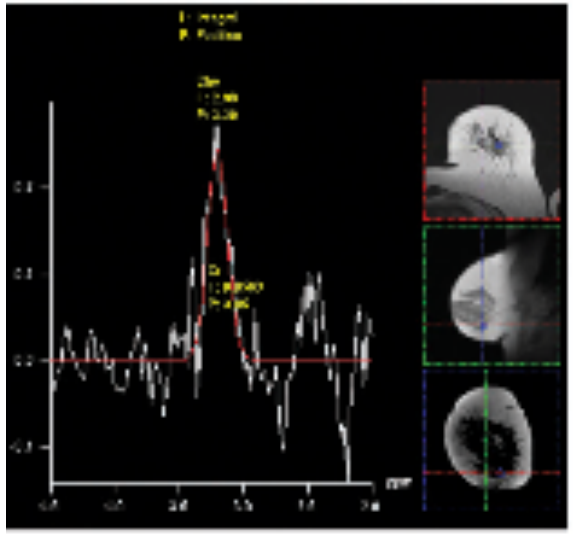

c.

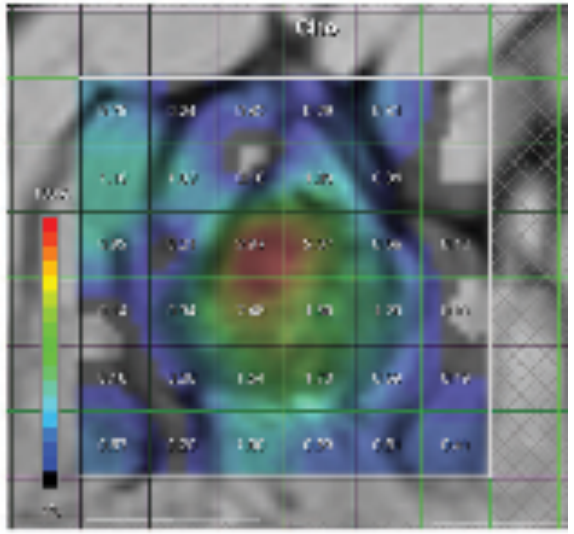

d.

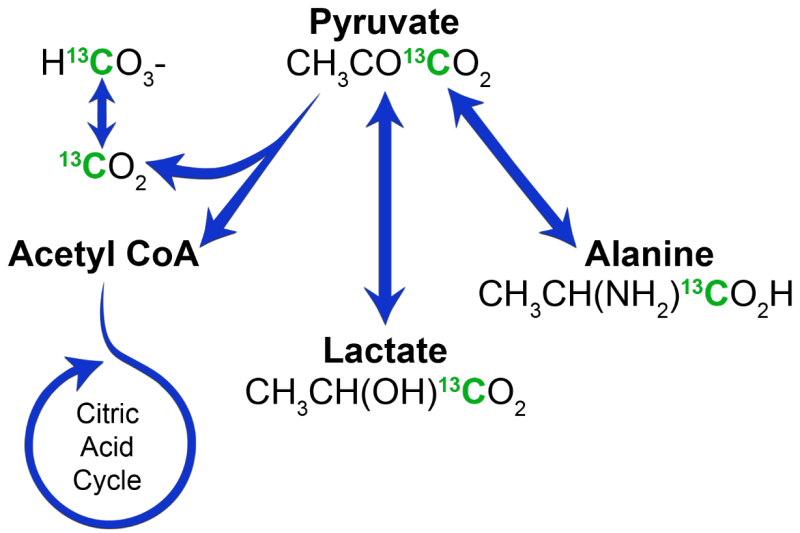
Pyruvate
$CH_3CO^{13}CO_2$
$H^{13}CO_3$-
$^{13}CO_2$
Acetyl CoA
Alanine
$CH_3CH(NH_2)^{13}CO_2H$
Lactate
$CH_3CH(OH)^{13}CO_2$
Citric
Acid
Cycle

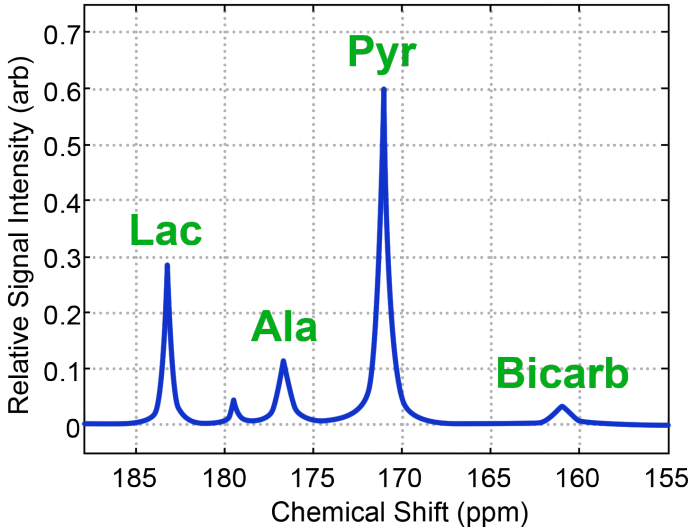
Relative Signal Intensity (arb)
0.7
0.6
0.5
0.4
0.3
0.2
0.1
0
Lac
Ala
Pyr
Bicarb
185
180
175
170
165
160
155
Chemical Shift (ppm)

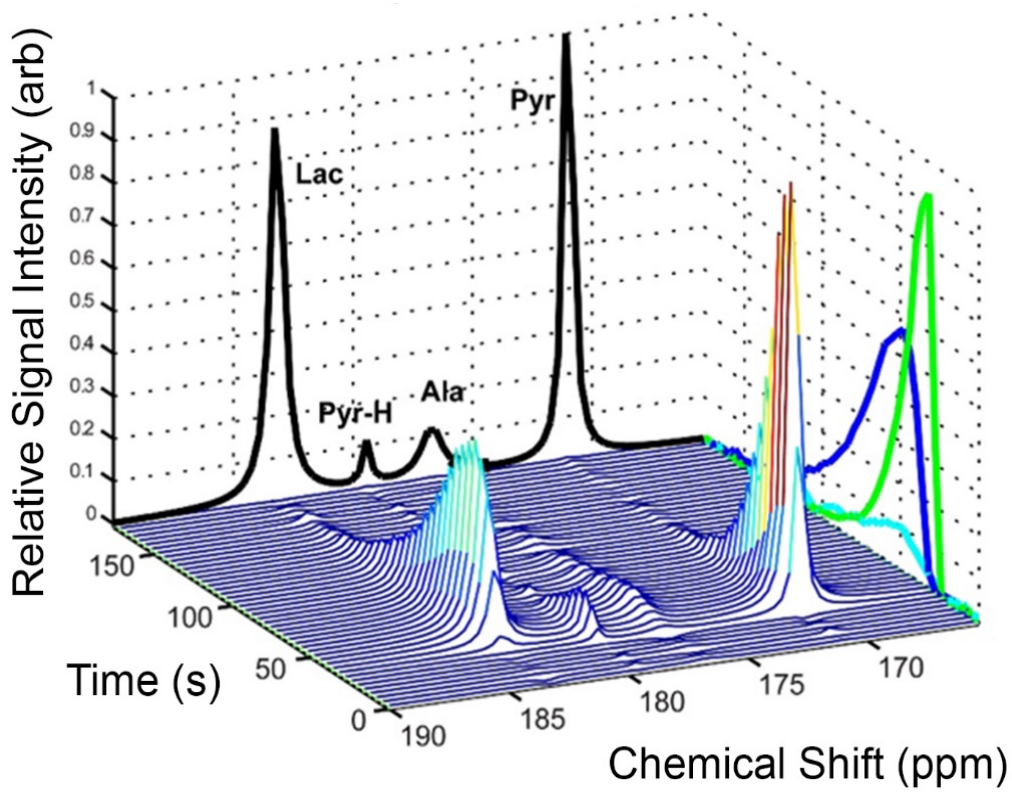
Relative Signal Intensity (arb)
1
0.9
0.8
0.7
0.6
0.5
0.4
0.3
0.2
0.1
0
Lac
Pyr
Pyr-H
Ala
150
100
50
0
Time (s)
190
185
180
175
170
Chemical Shift (ppm)

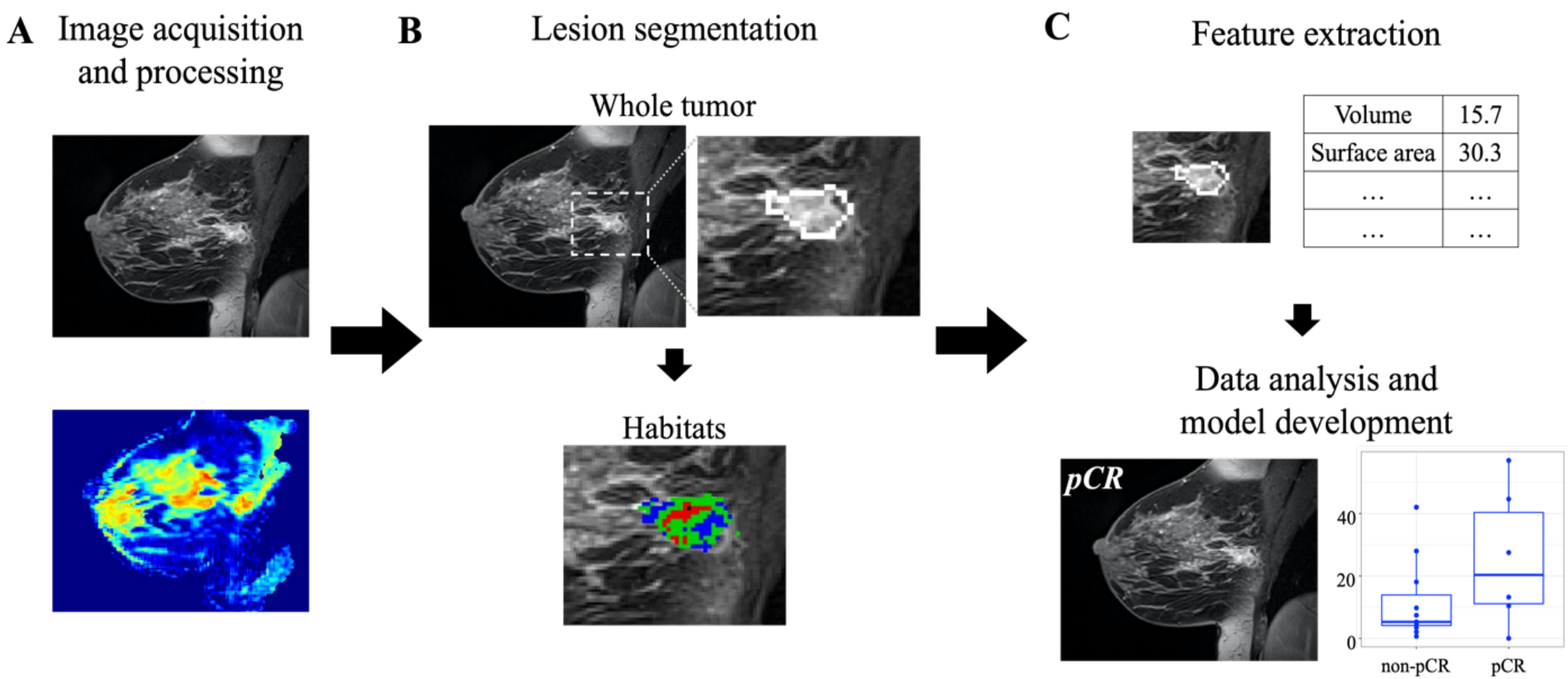
A
Image acquisition and processing
B
Lesion segmentation
Whole tumor
Habitats
C
Feature extraction
Volume 15.7
Surface area 30.3
… …
… …
Data analysis and model development
pCR
40
20
0
non-pCR
pCR

Data processing

- Using DW-MRI data (a) calculate the apparent diffusion coefficient map (c)
- Approximate tumor cellularity using apparent diffusion coefficient map using standard methods (f)
- Use DCE-MRI (b) to identify tumor ROIs (d)
- Analyze DCE-MRI data (c) with standard quantitative methods to identify physiological parameters of the vasculature (e)
- Approximate drug concentration in the tumor tissue per patient therapy regimens (g)

Mathematical model calibration and simulation

- Initialize and constrain the mathematical model using derived quantities.
- Calibrate the model's parameters using data early in the course of therapy.
- Generate patient specific predictions for the completion of therapy regimens